NEUROSCIENCE

Prickle promotes the formation and maintenance of glutamatergic synapses by stabilizing the intercellular planar cell polarity complex

Yue Ban, Ting Yu, Bo Feng, Charlotte Lorenz, Xiaojia Wang, Clayton Baker, Yimin Zou*

Whether there exists a common signaling mechanism that assembles all glutamatergic synapses is unknown. We show here that knocking out *Prickle1* and *Prickle2* reduced the formation of the PSD-95–positive glutamatergic synapses in the hippocampus and medial prefrontal cortex in postnatal development by 70–80%. *Prickle1* and *Prickle2* double knockout in adulthood lead to the disassembly of 70 to 80% of the postsynaptic-density(PSD)-95–positive glutamatergic synapses. PSD-95–positive glutamatergic synapses in the hippocampus of *Prickle2*$^{E8Q/E8Q}$ mice were reduced by 50% at postnatal day 14. Prickle2 promotes synapse formation by antagonizing Vangl2 and stabilizing the intercellular complex of the planar cell polarity (PCP) components, whereas Prickle2 E8Q fails to do so. Coculture experiments show that the asymmetric PCP complexes can determine the presynaptic and postsynaptic polarity. In summary, the PCP components regulate the assembly and maintenance of a large number of glutamatergic synapses and specify the direction of synaptic transmission.

INTRODUCTION

Glutamatergic synapses are the main excitatory synapses in the mammalian brain, and their normal formation and function are critical to brain function (*1*–*5*). Despite the tremendous diversity of glutamatergic synapses in terms of their connectivity, morphology, and electrophysiological properties, they have a common structural design, typically with a prominent postsynaptic density, dendritic spine, and highly organized presynaptic active zone (*4*–*7*). Extensive efforts have been made to study how this exquisite structure is assembled and regulated, and many signaling cascades, such as neurotrophin signaling, have been found to affect synapse formation, especially dendritic spine formation (*8*). However, whether all glutamatergic synapses are assembled by a common signaling mechanism, operating locally in the synapses, or by many different alternative pathways is not clear. Synaptic adhesion molecules have been studied extensively and are important for the function and, in some cases, the specificity of synaptic connections (*9*, *10*). They are typically not essential for glutamatergic synapse formation, because synapse formation is either not affected or only mildly affected in vivo even in straight knockouts (*9*, *11*, *12*). Therefore, the signaling mechanism that directly assembles glutamatergic synapses has been missing, leading to the question whether a common pathway even exists.

The planar cell polarity (PCP) is a promising candidate for such a common pathway (*13*). The PCP pathway, establishing tissue and cell polarity along the plane of the tissue, is highly conserved from *Drosophila* to mammals, involving six core components, including Frizzled (Fzd), Flamingo (named Celsrs in vertebrates), Van Gogh (named Vangls in vertebrates), Dishevelled (Dvl), Prickle, and Diego. These core PCP signaling components not only form complexes that are localized asymmetrically and antagonize each other within the same cell but also form asymmetric intercellular complexes between neighboring cells. The intracellular antagonism and intercellular communication are both important for establishing and maintaining planar polarity along the entire tissue. PCP components were found to be asymmetrically localized at developing glutamatergic synapses in similar fashion as in epithelial cell-cell junctions being planar polarized (*14*). Fzd3 is enriched on the presynaptic membrane, and Vangl2 is enriched on the postsynaptic membrane. Celsr3, a homophilic adhesion G protein–coupled receptor, is on both presynaptic and postsynaptic membranes. Celsr3 and Vangl2 play opposite roles in the assembly of glutamatergic synapses. Using conditional knockouts in pyramidal neurons, *Celsr3* was found required for the formation of 50% of the glutamatergic synapses in the hippocampus (HPC), as shown by electron microscopy and electrophysiology, whereas *Vangl2* inhibits synapse formation (*14*).

Whether PCP signaling is required for all glutamatergic synapses formation and whether it is also required for synapse maintenance in the mature neural circuits are not known. In addition, it is not known whether and how other core PCP components are directly involved in glutamatergic synapse formation. Here, using CRISPR-Cas9–mediated knockouts and conditional knockouts, we show that when *Prickle1 (PK1)* and *Prickle2 (PK2)* are both knocked out at postnatal day 7 (P7) or in adulthood (8 weeks old), PSD-95–positive synapse numbers were reduced by 70 to 80% in the HPC and medial prefrontal cortex (mPFC) at P21 and 12 weeks, respectively. Using CRISPR-Cas9–mediated gene editing, we generated a mouse line carrying a point mutation of *PK2 (E8Q)* found in human patients of autism (*15*). In *PK2*$^{E8Q/E8Q}$ animals, PSD-95–positive glutamatergic synapse numbers were found reduced by 50% at P14, and compositions of the postsynaptic density were altered, particularly with a large reduction of several members of the membrane-associated guanylate kinase (MAGUK) superfamily and the glutamate receptor subunits. We further show that PK2 promotes synapse formation by antagonizing Vangl2, which disrupts the asymmetric intercellular PCP complex made between Celsr3/Fzd3 on the membrane of one cell and Celsr3 on the other neighboring cell. The PK2 E8Q mutant protein is unstable and not able to stabilize this complex, which is essential for PCP signaling. More notably, human

Neurobiology Section, Biological Sciences Division, University of California, San Diego, La Jolla, CA 92093, USA.
*Corresponding author. Email: yzou@ucsd.edu

embryonic kidney (HEK) cells expressing Celsr3/PK2 can increase the accumulation of the presynaptic marker, Bassoon, on the dendrites contacting the HEK cells, whereas HEK cells expressing Celsr3/Fzd3/Dvl1 can increase the accumulation of the postsynaptic marker, PSD-95 on the axons contacting the HEK cells. These results suggest that the asymmetric signaling property of PCP components determines the direction of the presynaptic and postsynaptic organization to establish the direction of synaptic transmission.

RESULTS

PK1 and *PK2* are required for the formation and maintenance of 70 to 80% of the PSD-95–positive glutamatergic synapses in development and adulthood

PKs are core PCP components and asymmetrically localized on the proximal membranes of the distal cells in the junctions that are planar polarized (*13*). In mammals, there are four Prickles. PK1 and PK2, which share similar domain structures, are abundantly and broadly expressed in the nervous system in multiple brain regions. We carried out a number of studies to characterize the localization of PK1 and PK2 in glutamatergic synapses in development and adulthood. First, we found that PK1 and PK2, together with Celsr3 and Fzd3, maintain relatively constant levels of expression in the synapses in the cortex and HPC throughout development and till adulthood, whereas Vangl2 levels in the synapses appear to decrease during the first 5 months of the animals' life (fig. S1A); second, subcellular fractionation of synaptosome preparations from P21 wild-type (WT) mouse cortex showed that both PK1 and PK2 were highly enriched in the core PSD fraction (fig. S1, B and C); third, to directly analyze whether PK1 and PK2 localize in the same compartment with PSD-95, we performed imaging using the super-resolution microscopy, Three-dimensional (3D) Stochastic Optical Reconstruction Microscopy (3D-STORM) in the stratum radiatum (SR) of the HPC (*16*–*18*). We observed that both PK1 and PK2 were predominantly colocalized with the postsynaptic marker, PSD-95, but not with the presynaptic marker, Bassoon (Fig. 1A and movies S1 to S4); last, we asked whether PK1 and PK2 may have overlapping localization and functions in the synapses. Because the specific PK1 and PK2 antibodies are both rabbit antibodies, we used a sequential immunohistochemistry approach. For this, we would need four fluorophores to label PK1, PK2, a presynaptic marker, and a postsynaptic marker. Unfortunately, the signal from the 405-nm fluorophore got photobleached more easily than other the fluorophores in our hands (488, 568/594, and 647 nm). As a result, we could only costain three synaptic proteins, and we chose to stain PK1 and PK2 with the postsynaptic marker, PSD-95, as PKs are localized in the PSD. We found that, in hippocampal CA1 and the mPFC, respectively, 44.79 and 45.99% of the PK2 puncta were colocalized with either PK1, PSD-95, or both. PK1 puncta (74.25 and 72.5% in CA1 and mFPC, respectively) were colocalized with either PK2, PSD-95, or both. Most of the PSD-95 puncta (68.22 and 67.17%) were colocalized with either PK1, PK2, or both. (Fig. 1, B and C). Because not all PSD-95 puncta are in the synapses, the percentage of PSD-95 puncta colocalized with PKs does not represent the percentage of synapses that have PKs. Although we were not able to pinpoint the exact information of how PK1 and PK2 are colocalized in synapses, we conclude that there is a considerable overlap of the distribution of PK1 and PK2 in synapses.

We then examined the role of PK1 and PK2 in glutamatergic synapse formation during development and their maintenance in adulthood using the CRISPR-Cas9 system (*19*). Two sets of single guide RNAs (sgRNAs) were designed for *PK1*, and two sets of sgRNAs were designed for *PK2*. They were cloned into the adeno-associated virus (AAV)-U6-sgRNA-hSyn-Cre vector backbone and packaged (fig. S2, A and G). These sgRNA viruses efficiently eliminated the expression of *PK1* and *PK2* both in cultured hippocampal neurons and in vivo (fig. S2, B, C, H, and I). Because PCP signaling is important for the guidance of many classes of axons, we need to knockout *PKs* after axon development is finished to avoid secondary and indirect effects on synapse formation, which occurs after axon guidance. Therefore, we injected AAV-U6-sgRNA-hSyn-Cre into HPC and mPFC of the Cre-dependent Cas9 mice at P7. The efficiency of viral infection and Cre recombination was documented by the Cre-dependent expression of the green fluorescent protein (GFP) in the Cas9 mice at P21 (Fig. 1D). We then quantified the number of glutamatergic synapses using immunostaining with presynaptic (Bassoon) and postsynaptic (PSD-95) markers (Fig. 1, E and G, and fig. S2, D and J) and observed an average of 58.5% reduction in the number of synapses in *PK1* knockout (CA1 SR: sgPK1-1 = 64%, sgPK1-2 = 63%; mPFC: sgPK1-1 = 53%, sgPK1-2 = 54%) and an average of 43.5% decrease in *PK2* knockout (CA1 SR: sgPK2-1 = 40%, sgPK2-2 = 48%; mPFC: sgPK2-1 = 38%, sgPK2-2 = 48%) (Fig. 1, F and H, and fig. S2, E, F, K, and L). These results suggest that both *PK1* and *PK2* are required for synapse formation during development. To address whether *PK1* and *PK2* are also engaged in regulating the number of glutamatergic synapses in adulthood, we injected sgRNA viruses into the same brain regions of the Cre-dependent Cas9 mice at the age of 8 to 9 weeks. At 12 weeks, we found *PK1* deletion led to an average of 41.5% reduction (CA1 SR: sgPK1-1 = 29%, sgPK1-2 = 48%; mPFC: sgPK1-1 = 46%, sgPK1-2 = 43%), and *PK2* deletion resulted in an average of 57.5% reduction (CA1 SR: sgPK2-1 = 43%, sgPK2-2 = 66%; mPFC: sgPK2-1 = 57%, sgPK2-2 = 64%) (Fig. 1, I to L, and fig. S2, D to F, and J to L). Thus, *PK1* and *PK2* are critical not only for the assembly of glutamatergic synapses but also for their maintenance in adulthood. To examine whether *PK1* and *PK2* are functionally overlapping, we performed double knockout by injection of both the PK1 sgRNA virus and the PK2 sgRNA virus to the dorsal HPC and mPFC of the Cre-dependent Cas9 knock-in mice. Double knockout caused an average reduction of 72.5 and 75% during development and adulthood, respectively (reduction level of P7 deletion, CA1 SR: 76%, mPFC: 69%; reduction level of adult deletion, CA1 SR: 67%, mPFC: 83%) (Fig. 1, E to L). Thus, double knockout of both *PK1* and *PK2* led to a further reduction in the number of synapses during development and adulthood. We wondered whether the reduction of large numbers of synapses in HPC and mPFC may affect the survival of neurons and thus analyzed the level of cleaved caspase-3 (CC3), a marker for apoptosis. We observed a trend of increase in the number of cells expressing CC3 2 weeks after knocking out both *PK1* and *PK2* at P7. In adulthood, a statistically-significant increase in the population of CC3-positive cells was found 3 weeks after receiving the PK1 and PK2 sgRNA virus injection at 8 weeks of age (fig. S3). It is possible that the survival of neurons is less dependent on synapses during development than in adulthood. The reason that we did not observe massive apoptosis in adult knockout may be because the remaining synapses are sufficient for neurons to survive, or other PSD-95–negative

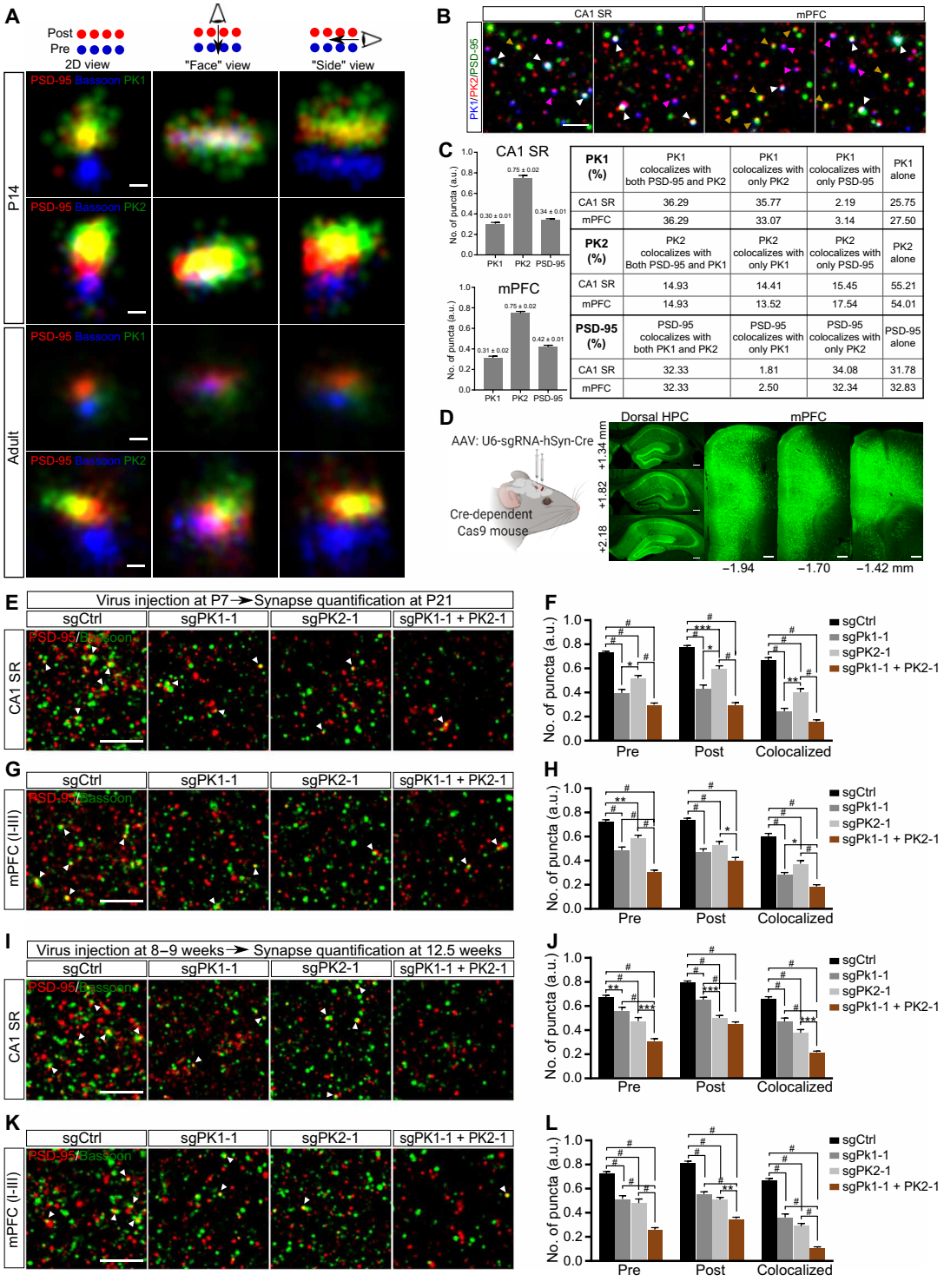

Fig. 1. Double knockout of *PK1* and *PK2* on P7 and in adulthood resulted in 70 to 80% reduction of the numbers of the PSD-95–postive glutamatergic synapses. (**A**) Representative 3D STORM images showing localization of PK1 (green), PK2 (green) with the presynaptic marker Bassoon (blue), and the postsynaptic marker PSD-95 (red) in CA1 SR of P14 and adult WT mice. Scale bars, 0.1 μm. (**B**) Localization of PK1 (blue) and PK2 (red) in glutamatergic synapses, marked by PSD-95 (green), in CA1 SR and mPFC at P10. Scale bar, 2 μm. White arrowheads indicate clusters containing colocalized PK1, PK2, and PSD-95. Yellow arrowheads represent clusters containing only PK2 and PSD-95. Magenta arrowheads point to clusters containing only PK1 and PK2. (**C**) Quantification of the number of PK1, PK2, and PSD-95 puncta and the number of colocalized puncta. (**D**) Validation of viral injection and Cre recombination. Scale bars, 200 μm. (**E** to **L**) Immunostaining with synaptic markers and quantifications of synapse numbers. Glutamatergic synapses are identified by colocalization of presynaptic (green; Bassoon) and postsynaptic (red; PSD-95) markers. Arrowheads indicate colocalized puncta. Scale bars, 5 μm. Data were normalized by dividing each value to the maximum value in each independent experiment. Kruskal-Wallis test was used to compare the means of the four groups, and Dunn's test was used to perform multiple comparisons. *$P < 0.05$, **$P < 0.01$, ***$P < 0.001$, and #$P < 0.0001$. Error bars represent SEM. a.u., arbitrary units.

synapses were not affected as much. It is also possible that more cell death may occur if we waited longer than 3 weeks. However, we did notice a trend of reduced body weight in the double knockouts (fig. S2, M and N).

Last, to independently validate our findings about synapse numbers, we analyzed dendritic spine density using the *PK1* and *PK2* conditional alleles, which we generated using the CRISPR-Cas9 system. Two LoxP elements were inserted in two introns flanking the exon2 where the start codons are located (Fig. 2, A and B). The two LoxP sites were inserted in cis orientation with correct sequences (fig. S4, A and B), and Western blot was performed to confirm the loss of PK1 and PK2 protein expression in the conditional knockout (cKO) mice (fig. S4, C and D). To avoid potential off-target effects, we backcrossed *PK1* and *PK2* conditional alleles to *WT* B6 background for six to seven generations before we analyzed the phenotypes in details. We then injected a mixture of diluted AAV: hSyn-Cre (1:5000) with AAV: CAG-Flex–enhanced GFP (eGFP) into the dorsal HPC and mPFC of the *PK1* and *PK2* cKO mice to knockout *PKs* and also sparsely label neurons to analyze synapse numbers by imaging the dendritic spines (fig. S4, E and F). Conditional deletion of either *PK1* or *PK2* led to a significant decrease in the density of dendritic spines during development and in adulthood. *PK1* cKO and *PK2* cKO at P7 led to 33 and 44% reduction of the dendritic spines on the apical dendrites of the CA1 pyramidal neurons, respectively, and 26 and 43% reduction of the dendritic spines on the distal dendrites of the mPFC pyramidal neurons, respectively. In adulthood, *PK1* cKO and *PK2* cKO in HPC resulted in 30 and 36% reduction of the dendritic spines on the apical dendrites of the CA1 pyramidal neurons, respectively, and 41 and 38% reduction of dendritic spines on the distal dendrites of the mPFC pyramidal neurons, respectively. (Fig. 2, C to J). We have not been able to obtain *PK1/PK2* double cKO mice and thus do not have the data for the reduction of synapse numbers in the double cKO. However, the extent of the reduction of synapse numbers caused by *PK1* and *PK2* single cKO, assessed by spine density, is comparable with the that assessed by immunostaining with synaptic markers in the earlier Cas9/sgRNA approach (Fig. 1, E to L). Together, our results demonstrate that *PK1* and *PK2* are required for the assembly and maintenance of 70 to 80% of the PSD-95–positive glutamatergic synapses.

The $PK2^{E8Q/E8Q}$ mice showed reduced synaptic density and altered spatial learning

A large number of *PK* mutations are associated with autism and epilepsy in humans and may provide clues to the function and mechanisms of *PKs* in synapse formation and maintenance (*15*, *20*–*24*). The *PK2 E8Q* mutation was identified in a family with autism spectrum disorder, suggesting that this amino acid may be critical for the function of PK2 (*15*). We used CRISPR-Cas9–mediated gene editing to generate mice carrying the *PK2 E8Q* mutation (Fig. 3A). Polymerase chain reaction (PCR) and DNA sequencing confirmed the point mutation (Fig. 3, B and C). To avoid potential off-target effects, we backcrossed *PK2 E8Q* to WT B6 background for six to seven generations before we analyzed phenotypes in details. We first performed immunostaining with synaptic markers to examine the number of glutamatergic synapses in the SR of the CA1 of the P14 *PK2* mutant animals and their WT littermates (Fig. 3D). A large (~50%) reduction in the number of synapses was found in the *P14* $PK2^{E8Q/E8Q}$ mice (Fig. 3E). We then performed behavioral analyses of adult animals and found that, in adulthood, *PK2* mutant mice showed normal locomotor activity and no anxiety in the open-field task or light-dark transition task (fig. S5, A to D). However, we observed deficits in the Barnes maze task for spatial learning and memory. During the acquisition training, the $PK2^{E8Q/E8Q}$ mice spent significantly longer time to locate the real escape hole in the two trials on the first day, but they caught up in the following trials and were able to locate the real escape hole as fast as the heterozygous and WT littermates on the last day of training (Fig. 3G). In the probe test to evaluate spatial memory, the $PK2^{E8Q/E8Q}$ mice spent significantly longer time in the target quadrant housing the original escape hole than the heterozygous and WT littermates (Fig. 3H), suggesting that the $PK2^{E8Q/E8Q}$ mice have either better spatial memory or difficulty in changing a learned pattern. To distinguish these possibilities, we continued the Barnes maze task with a reversal training phase, during which the new escape hole was located 180° opposite to the original escape hole. $PK2^{E8Q/E8Q}$ mice, but not the heterozygous and WT littermates, displayed impaired behavioral flexibility shown by the longer latency to locate the new escape hole on the first day of the reversal training (Fig. 3I). We analyzed the synapse numbers in another cohort of $PK2^{E8Q/E8Q}$ mice in adulthood and found that the synapse numbers in $PK2^{E8Q/+}$ and $PK2^{E8Q/E8Q}$ have both recovered to be similar to the WT littermates (Fig. 3, D and F). This may be because the *PK2 E8Q* mutant protein was eventually able to make the correct number of synapses in adulthood, although it was less efficient initially. It is also possible that the recovery may be mediated by *PK1* or other PKs, such as *PK3*. Therefore, the behavioral deficits in *PK2 E8Q* are likely caused by altered synapse function but not by synapse numbers and synapse function or plasticity is likely more affected in homozygous mutants than in the heterozygous mutants.

The $PK2^{E8Q/E8Q}$ mice showed altered composition of synaptic proteins, including glutamate receptors, MAGUK proteins, PCP components, and a regulator of PCP, Mink1

To understand how the *PK2* point mutation (*E8Q*) may affect synaptic function, we first analyzed the composition of synaptic proteins by Western blot. We assessed the levels of the core PCP components and some of the key PSD proteins (*25*). We extracted the synaptosome fraction from the cortex and HPC of P14 mice and found that the mutant PK2 protein level was significantly reduced in the $PK2^{E8Q/E8Q}$ mice (Fig. 4, A and D). In contrast, the level of Vangl2 in the synaptosome fraction was increased in the $PK2^{E8Q/E8Q}$ mice, which is consistent with a negative role of Vangl2 in controlling synapse numbers (Fig. 4, A and D). Celsr3 level was unchanged (Fig. 4, A and D). We also performed preliminary mass spectrometry with the core PSD proteins and found that Mink1, which phosphorylates PK and regulates the localization of Vangl-PK complex, was decreased in the core PSD fraction from the $PK2^{E8Q/E8Q}$ mice at P21 (*26*). We were able to confirm the reduction of the Mink1 protein level in the synaptosome fraction (Fig. 4, A and D). We also detected a reduction in the levels of AMPA receptor subunits glutamate receptor 1 (GluR1) and glutamate receptor 2 (GluR2) NMDA receptor subunits N1 and NMDA receptor 2B (NR2B) (Fig. 4, B and E). Although *PK2 E8Q* mutation did not seem to affect the level of PSD-95, we observed a significant reduction in the level PSD-93 and synapse-associated protein 97 (SAP-97) in the synaptosome fraction of $PK2^{E8Q/E8Q}$ mice (Fig. 4, C and F). Next, we performed immunofluorescence staining of PK2 and Vangl2 in P14 mouse brain sections and observed significant reduction in the

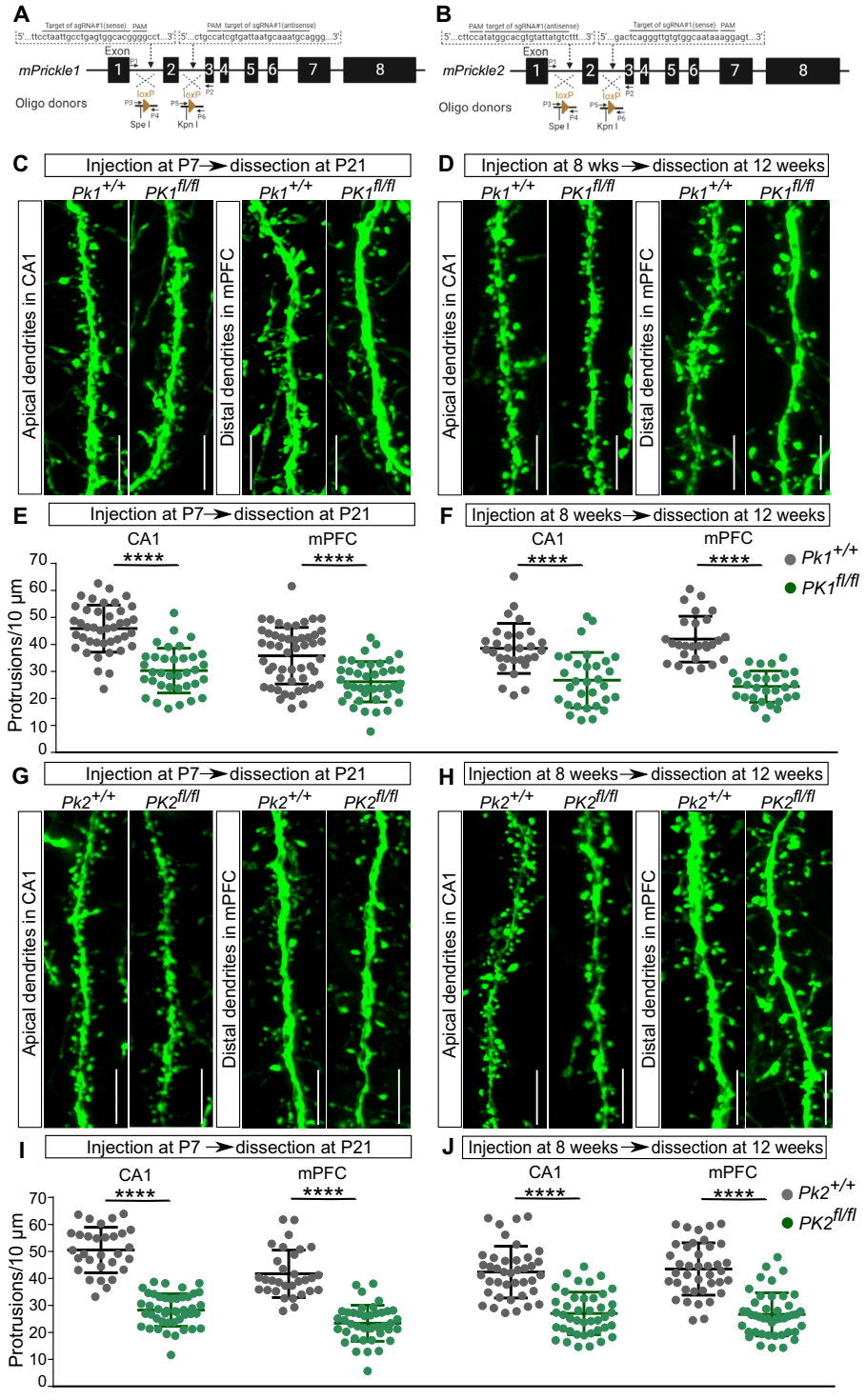

Fig. 2. Conditionally knocking out *PK1* or *PK2* led to large decreases of synapse formation in development and synapse numbers in adulthood. (**A** and **B**) Schematic of the designs of the *PK1* and *PK2* cKO mice using the CRISPR-Cas9 system. (**C** to **F**) Density of dendritic spines after *PK1* conditional KO in the dorsal HPC and mPFC at P7 or at 8 weeks of age. For deletion at P7, CA1 apical dendrites: $PK1^{+/+}$, $n = 41$ dendritic segments; $PK1^{fl/fl}$, $n = 35$ dendritic segments; distal dendrites of mPFC pyramidal neurons: $PK1^{+/+}$, $n = 51$ dendritic segments; $PK1^{fl/fl}$, $n = 41$ dendritic segments. For deletion at 8 weeks of age, CA1 apical dendrites: $PK1^{+/+}$, $n = 29$ dendritic segments; $PK1^{fl/fl}$, $n = 31$ dendritic segments; distal dendrites of mPFC pyramidal neurons: $PK1^{+/+}$, $n = 27$ dendritic segments; $PK1^{fl/fl}$, $n = 29$ dendritic segments. (**G** to **J**) Density of dendritic spines after PK2 conditional KO in the dorsal HPC and mPFC at P7 or at 8 weeks of age. For deletion at P7, CA1 apical dendrites: $PK2^{+/+}$, $n = 30$ dendritic segments; $PK2^{fl/fl}$: $n = 44$ dendritic segments; distal dendrites of mPFC pyramidal neurons: $PK2^{+/+}$, $n = 31$ dendritic segments; $PK2^{fl/fl}$, $n = 40$ dendritic segments. For deletion at 8 weeks of age, CA1 apical dendrites: $PK2^{+/+}$, $n = 40$ dendritic segments; $PK2^{fl/fl}$, $n = 42$ dendritic segments; distal dendrites of mPFC pyramidal neurons: $PK2^{+/+}$, $n = 39$ dendritic segments; $PK2^{fl/fl}$, $n = 44$ dendritic segments. Student's *t* test, $^{****}P < 0.0001$. Scale bars, 5 μm. Error bars represent SD.

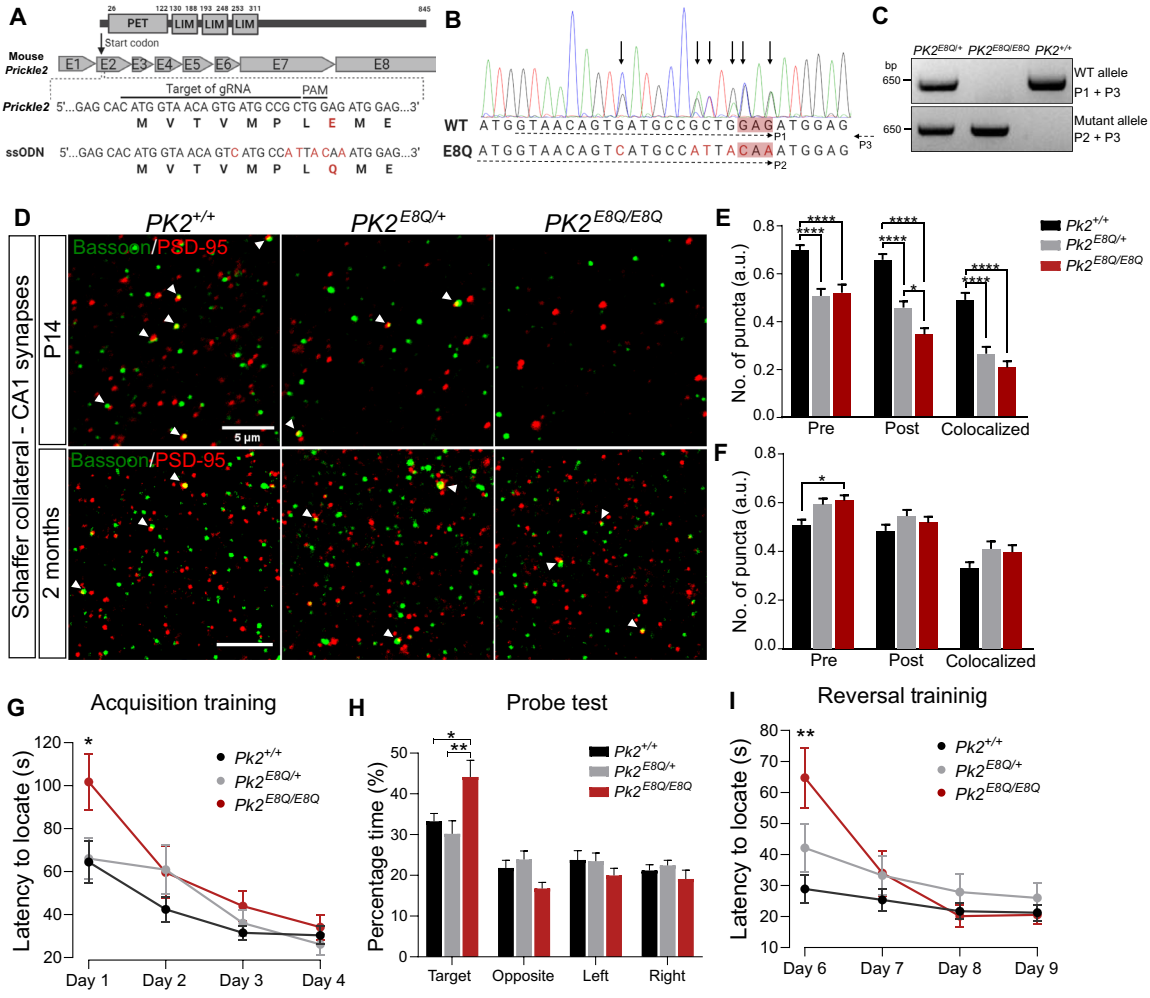

Fig. 3. The *PK2*$^{E8Q/E8Q}$ mice showed reduced numbers of excitatory synapses in development and impaired spatial learning in adulthood. (**A**) Generation of *PK2 E8Q*. Guide RNA (gRNA) target site and protospacer adjacent motif (PAM) sequence were indicated. Additional synonymous mutations (highlighted in red) were generated in ssODN to prevent Cas9 protein from cleaving the target site after homology-directed repair. (**B**) Sequencing confirms the presence of both WT allele and mutant allele in a *PK2*$^{E8Q/+}$ mice. (**C**) PCR and gel electrophoresis to determine the genotypes. (**D** and **E**) Quantification of synapse numbers in CA1 SR at P14 and 2 months. Green, Bassoon; red, PSD-95. Arrowheads indicate colocalized puncta. (E) Quantification of synapse numbers. Eighty images from six *PK2*$^{+/+}$, 60 images from four *PK2*$^{E8Q/+}$, and 52 images from four *PK2*$^{E8Q/E8Q}$. (**F**) Quantification of synapse numbers. One hundred three images from five *PK2*$^{+/+}$, 61 images from three *PK2*$^{E8Q/+}$, and 79 images from four *PK2*$^{E8Q/E8Q}$. Scale bars, 5 µm. Kruskal-Wallis test was used to compare the means of three groups, and Dunn's test was used to perform multiple comparisons. (**G**) The latency in locating the escape hole on the first day of the acquisition training. *PK2*$^{+/+}$, $n = 17$; *PK2*$^{E8Q/+}$, $n = 17$; *PK2*$^{E8Q/E8Q}$, $n = 17$. (**H**) The time in the target quadrant housing the original escape hole in the probe test. *PK2*$^{+/+}$, $n = 16$; *PK2*$^{E8Q/E8Q}$, $n = 15$. (**I**) Time spent locating the new escape hole. *PK2*$^{+/+}$, $n = 17$; *PK2*$^{E8Q/+}$, $n = 17$; *PK2*$^{E8Q/E8Q}$, $n = 16$. One-way ANOVA, $^{*}P < 0.05$, $^{**}P < 0.01$, and $^{****}P < 0.0001$. Error bars represent SEM.

number and the average size of PK2 puncta but a significant increase in the average size of Vangl2 puncta in the SR in CA1 (Fig. 4, G to K). Therefore, the synaptic protein composition and synaptic structure are altered, consistent with the altered behavior (Fig. 3, G to I).

PK2 promotes glutamatergic synapse formation by antagonizing Vangl2 and stabilizing the intercellular complex Celsr3/Fzd3-Celsr3

Our results show that PKs are required for the formation and maintenance of a large majority of the PSD-95–positive synapses. We then asked whether PKs promote synapse formation using the well-established HEK293T cell–hippocampal neuron mixed culture assay (Fig. 5A) (*27*). We measured the density of Bassoon on axons that contact the HEK293T cells but are not localized with dendrites. Expression of Celsr3 in HEK293T cells led to a significant increase in the density of Bassoon on isolated axons contacting the transfected HEK293T cell (Fig. 5, C and H). Although PK2 alone had no effect on the density of axonal Bassoon (Fig. 5, D and H), Celsr3 and PK2 together greatly increased the accumulation of axonal Bassoon (Fig. 5, F and H). Another core PCP component Vangl2 was shown to be a negative regulator of synapse formation (*14*). Consistently, we found that cotransfection of Celsr3 and Vangl2 reduced the accumulation of axonal Bassoon compared to Celsr3 alone (Fig. 5, E and H). Cotransfection PK2 with Celsr3 and Vangl2 restored the accumulation of Bassoon (Fig. 5, G and H), suggesting that PK2 may promote synapse formation by antagonize the inhibitory role of Vangl2 (*14*).

PCP components function by forming intercellular protein complexes at cell-cell junctions to transduce directional information

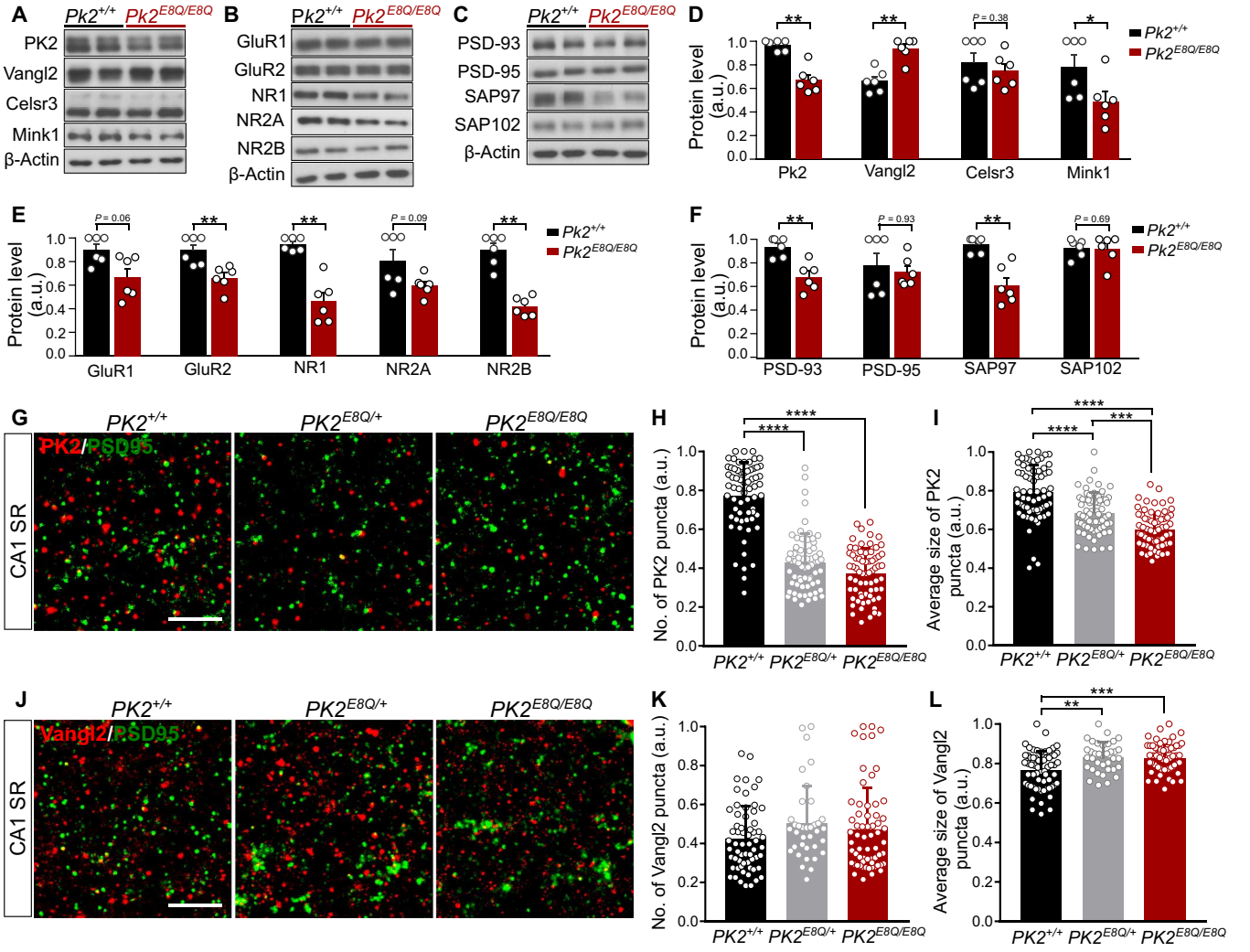

Fig. 4. Altered composition of synaptic proteins in the *PK2*$^{E8Q/E8Q}$ mice. (**A** to **C**) Western blot analysis of PCP components, regulator of PCP signaling, Mink1, alpha-amino-3-hydroxy-5-methyl-4-isoxazole propionic acid receptor (AMPAR)/N-methyl-D-aspartate receptor (NMDAR) subunits, and MAGUK family proteins in the crude synaptosomes of cortex and HPC from P14 *PK2*$^{E8Q/E8Q}$ mice and WT littermates. (**D** to **F**) Quantitation of protein levels shown in (A) to (C). Each data point represents one animal. Data were normalized by dividing each value to the maximum value in each independent experiment. *PK2*$^{+/+}$, $n = 6$; *PK2*$^{E8Q/E8Q}$, $n = 6$, Mann-Whitney *U* test, $^{*}P < 0.05$ and $^{**}P < 0.01$. Error bars represent SEM. (**G** to **L**) Immunofluorescence staining of PK2 and Vangl2 in CA1 SR of P14 mice. To quantify the number (H) and the average size (I) of PK2 puncta, 66 image stacks of CA1 SR were taken from three *PK2*$^{+/+}$ animals, 66 image stacks from three *PK2*$^{E8Q/+}$ animals, and 68 image stacks from three *PK2*$^{E8Q/E8Q}$ animals. To quantify the number (K) and the average size (L) of Vangl2 puncta, 62 image stacks were taken from three *PK2*$^{+/+}$ animals, 36 image stacks from two *PK2*$^{E8Q/+}$ animals, and 63 image stacks from *PK2*$^{E8Q/E8Q}$ animals. Data were normalized by dividing each value to the maximum value in each independent experiment. Scale bars, 5 μm. Kruskal-Wallis test was used to compare the means of three groups, and Dunn's test was used to perform multiple comparisons. $^{**}P < 0.01$, $^{***}P < 0.001$, and $^{****}P < 0.0001$. Error bars represent SD.

across cells (*13*). Among these interactions, the Celsr3/Fzd3-Celsr3 intercellular interaction is important for synapse formation (*14*). Using a transcellular interaction assay, recently developed in our laboratory, we tested the role of PK2 in the Celsr3/Fzd3-Celsr3 intercellular interaction (*28*). Here, we transfected Celsr3 (not tagged) and Fzd3 [hemagglutinin (HA)–tagged] into HEK293T cells in one plate (cell A) and Celsr3 (Flag-tagged), with or without Myc-Vangl2/HA-PK2, in another plate (cell B). Twenty-four hours after transfection, we dissociated and mixed the cells from two plates and cultured the mixed cells for another 24 hours (Fig. 5I). To test whether this intercellular complex does exist, we performed immunocytochemistry and were able to detect the colocalization of Fzd3-HA and Celsr3-Flag from neighboring HEK293T cells (fig. S6). Cell lysate was then extracted and subjected to immunoprecipitation (IP) with anti-Flag antibodies and then Western blot with HA antibody to detect the intercellular complex. Vangl2 from Cell B markedly reduced Fzd3-Celsr3 intercellular interaction and PK2 in cell B antagonized Vangl2 and stabilized the Celsr3/Fzd3-Celsr3 intercellular complex (Fig. 5, J and K). Therefore, PK2 stabilizes the intercellular complex of Celsr3/Fzd3-Celsr3 by antagonizing Vangl2. Together, with the aforementioned culture assays (Fig. 5, A to H), we propose that PK2 may promote synapse formation by stabilizing the trans-synaptic complex of Celsr3/Fzd3-Celsr3 by antagonizing Vangl2. Although these assays were performed in transfected HEK

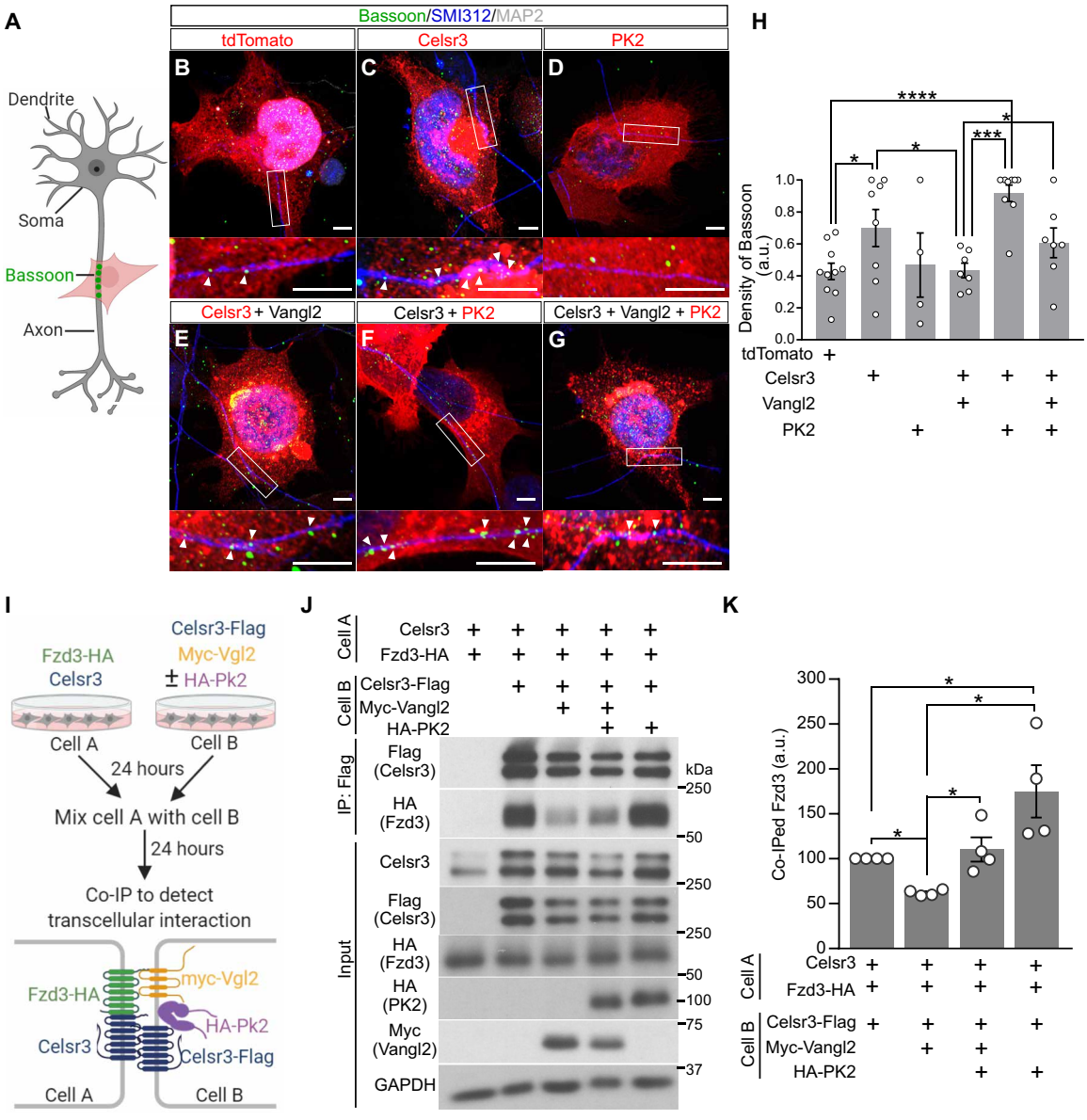

Fig. 5. PK2 promotes synapse formation by antagonizing Vangl2 and stabilizes the Celsr3/Fzd3-Celsr3 intercellular complex. (**A**) Schematic of the coculture assay with hippocampal neurons and HEK293T cells. (**B** to **H**) Effects of PCP proteins in synapse formation. HEK293T cells were transfected with indicated cDNA shown in the text boxes and cocultured with primary hippocampal neurons form DIV9 to DIV11. Representative images of transfected HEK cells contacting neuronal axons (blue, SMI312) but not dendrites (gray, MAP2) are shown in (B) to (G). tdTomato, negative control. Scale bars, 5 μm. The density of presynaptic marker Bassoon on axons contacting transfected HEK cells was measured. Each data point represents one independent experiment. In each experiment, 8 to 10 images were analyzed to calculate the mean value in each group. Data were normalized by dividing each value to the maximum value in each independent experiment. One-way ANOVA, $^{*}P < 0.05$, $^{***}P < 0.001$, and $^{****}P < 0.0001$. (**I**) Schematics of the transcellular interaction assay. HEK293T cells were seeded on separate plates and transfected with indicated PCP protein plasmids. Twenty-four hours after transfection, cells from two plates were dissociated, mixed, and cultured together. After 24 hours, total protein was prepared, and coimmunoprecipitation (co-IP) was performed to examine the intercellular interaction between Fzd3-HA from cell A and Celsr3-Flag from cell B. (**J**) The role of PK2 in regulating the stability of the Celsr3/Fzd3-Celsr3 intercellular complex. GAPDH, glyceraldehyde-3-phosphate dehydrogenase. (**K**) Quantification of (J). Each data point represents one independent experiment. Data were normalized by dividing each value to the value in the first group (cell A: Celsr3 + Fzd3-HA; cell B: Celsr3-Flag) in each independent experiment. One-way ANOVA, $^{*}P < 0.05$. Error bars represent SEM.

cells, we propose that similar interaction may occur in neuronal synapses. In addition, the in vivo phenotypes of *PK* mutations in Figs. 1 and 2 are consistent with our finding that PK2 promotes synapse formation by stabilizing the intercellular PCP complex.

The intercellular complexes of the PCP proteins have been shown essential by both genetic and biochemical studies in PCP signaling (*13*). For example, the intercellular interaction between Fzd and Van Gogh has been studied by both genetic and biochemical approaches in *Drosophila* (*29*). In this "transcellular interaction assay," cells transfected with different PCP components are mixed to mimic the asymmetric protein complexes. We used the similar cell mixing techniques to test the intercellular interactions between

Frlzzled3 and Vangl2, which is dynamically regulated by Fzd3 phosphorylation states (*28*). In that paper, we found that the interaction between Fzd3 and Vangl2 was greatly enhanced when both cells have Celsr3. In the subsequent experiments, we found that expressing LRRK2 or LRRK2 gain-of-function mutant in the cells that coexpress Fzd3 can alter the interaction between Fzd3 and Vangl2 (*28*). In another paper (in press at *Science Advances*) reporting the role of PCP signaling in synapse degeneration induced by amyloid β oligomers, we also used this assay to show that Vangl2 causes the reduction of the intercellular complex, and amyloid β oligomers enhance the function of Vangl2, which may cause the disassembly of synapses. We believe that this biochemical assay may reflect the intrinsic molecular interactions of the PCP components. In addition, we think mixed culture would provide a more consistent environment to test these protein-protein interactions than mixing the proteins together in a homogenate, as the mixed culture does mimic the in vivo PCP complex.

The PK2 E8Q protein is unstable and unable to stabilize the Celsr3/Fzd3-Celsr3 intercellular complex

To understand how PK2 promotes synapse formation, we further characterized the WT PK2 and the PK2 E8Q protein. First, we found that Celsr3 protected PK2 from the proteosome-mediated degradation induced by Vangl2 (Fig. 6, A to C) (*30*). Second, the PK2 E8Q protein is even more unstable than WT PK2 in the presence of Vangl2 (Fig. 6, D and E). Third, Pk2 E8Q failed to stabilize the intercellular Fzd3/Celsr3-Celsr3 complex in the same manner as WT PK2 (Fig. 6, F to H). Fourth, the level of co-immunoprecipitated (coIPed) PK2 E8Q with Vangl2 was higher than that of WT PK2 (Fig. 6, I and J), although the E8Q mutation did not alter the PK2-Celsr3 interaction (Fig. 6, I and J).

We performed a mass spectrometry analyses with PSD of the protein content changes in the *PK2 E8Q* mice. One of the PK-binding proteins, Mink1, was found significantly reduced, which we confirmed with Western blot with the synaptosome fraction (Fig. 4, A and B). We found here that the E8Q mutation did not affect the binding of PK2 with Mink1, but the protein levels of Mink1 were greatly reduced when cotransfected with PK2 E8Q (Fig. 6, K to N), suggesting that mutation of PK2 at E8Q also leads to the increased degradation of Mink1, which may explain the reduction of Mink1 levels in the synapses. Mink1 is required for PK function (*26*). Therefore, less Mink1 may represent weaker PK function. Although these biochemical assays were performed in transfected HEK cells and neuron-HEK cell cocultures, we propose that similar interactions may occur in neuronal synapses. In addition, the in vivo phenotypes of *PK2 E8Q* mutation in Figs. 3 and 4 are consistent with our finding that the PK2 E8Q protein is unstable and cannot stabilize the intercellular PCP complex.

PCP signaling components specify the presynaptic and postsynaptic polarity across the glutamatergic synapses

PCP signaling is known to polarize tissue and cells by creating asymmetric cell-cell junctions (*13*). We then asked whether PCP signaling components can specify the presynaptic and postsynaptic polarity across the glutamatergic synapses. First, we found that Vangl2 increased Celsr3-Pk2 interaction (Fig. 7, A and B), whereas PK2 reduced Celsr3-Vangl2 interaction (Fig. 7, C and D), suggesting that PK2 will eventually take over the interaction with Celsr3 resulting in the removal of Vangl2 in the complex. The Celsr3/PK2 complex is enriched on the postsynaptic membrane because PK2 is enriched on the postsynaptic side of the synapses. We tested whether the Celsr3/PK2 complex produces a signal to specify the postsynapse by asking whether Celsr3/PK2 can recruit presynaptic markers to a dendrite. We transfected HEK293T cells with tdTomato (negative control), Celsr3 alone, or Celsr3 with PK2, cocultured them with hippocampal neurons, and then quantified the density of the presynaptic marker Bassoon on the dendrites contacting the transfected HEK293T cells. To exclude the Bassoon puncta expressed on nearby axons, which are likely colocalized with postsynaptic protein PSD-95 on dendrites, we specifically measured the density of Bassoon puncta not colocalized with PSD-95. We found that HEK cells expressing Celsr3 and PK2 significantly elevated the density of Bassoon on dendrites contacting the HEK295T cells, whereas Celsr3 alone had no significant effect (Fig. 7, E to H). Last, we examined whether the presynaptic PCP complex, Fzd3/Dvl1, can recruit postsynaptic markers on axons. We transfected HEK cells with Celsr3 with Fzd3 and Dvl1, then cocultured with hippocampal neurons, and measured the density of PSD-95 on axons contacting the transfected HEK cells (but not contacting dendrites). Expression of Celsr3 together with Fzd3 and Dvl1 led to an accumulation of PSD-95 on the axons of cocultured hippocampal neurons contacting the HEK cells (Fig. 7, I to L). Together, our data show that PCP signaling complexes can specify the presynaptic and postsynaptic polarity of excitatory synapses in these assays using the neuron-HEK cell cocultures. Carefully designed genetic manipulations in a well-defined system to examine presynaptic and postsynaptic direction of synaptic transmission will be necessary to properly test this hypothesis in vivo. However, these in vitro culture results strongly support the role of PCP signaling components in synapse formation and maintenance.

DISCUSSION

Whether a common signaling mechanism directly regulates the assembly of all glutamatergic synapses is unknown. Our work shows that a core PCP component, PK, located in the PSD, is responsible for the formation and maintenance of 70 to 80% of the PSD-95–positive glutamatergic synapses in development and in adulthood. 70 to 80% of the PSD-95–positive glutamatergic synapses failed to form when *PK1* and *PK2* were knocked out 1 week after birth. 70 to 80% of the PSD-95–positive glutamatergic synapses were lost 1 month after *PK1* and *PK2* were knocked out at 8 weeks of age (Figs. 1 and 2, and fig. S2). We are currently not able to conclude whether PCP signaling components are responsible for the formation and maintenance of all glutamatergic synapses due to the following reasons: (i) Conditional knockout is not 100% efficient; (ii) it may take time for proteins to be degraded after the genes are knocked out; (iii) there are four Prickle genes in mouse, and Prickle3 is known to be expressed in the brain. Therefore, we do not know whether some of the 30% PSD-95 puncta not colocalized with either PK1 or PK2 are colocalized with Prickle3. Nor do we know whether Prickle3 is involved in synapse formation; (iv) in addition to the PSD-95–positive glutamatergic synapse, there are SAP-102–positive synapses (*4*, *5*). We currently do not know whether PCP pathway regulates the SAP-102–positive synapses.

We show that the asymmetric PCP complexes provide directional instruction to ectopically recruit the presynaptic marker, Bassoon, on dendrites and the postsynaptic marker, PSD-95, on axons,

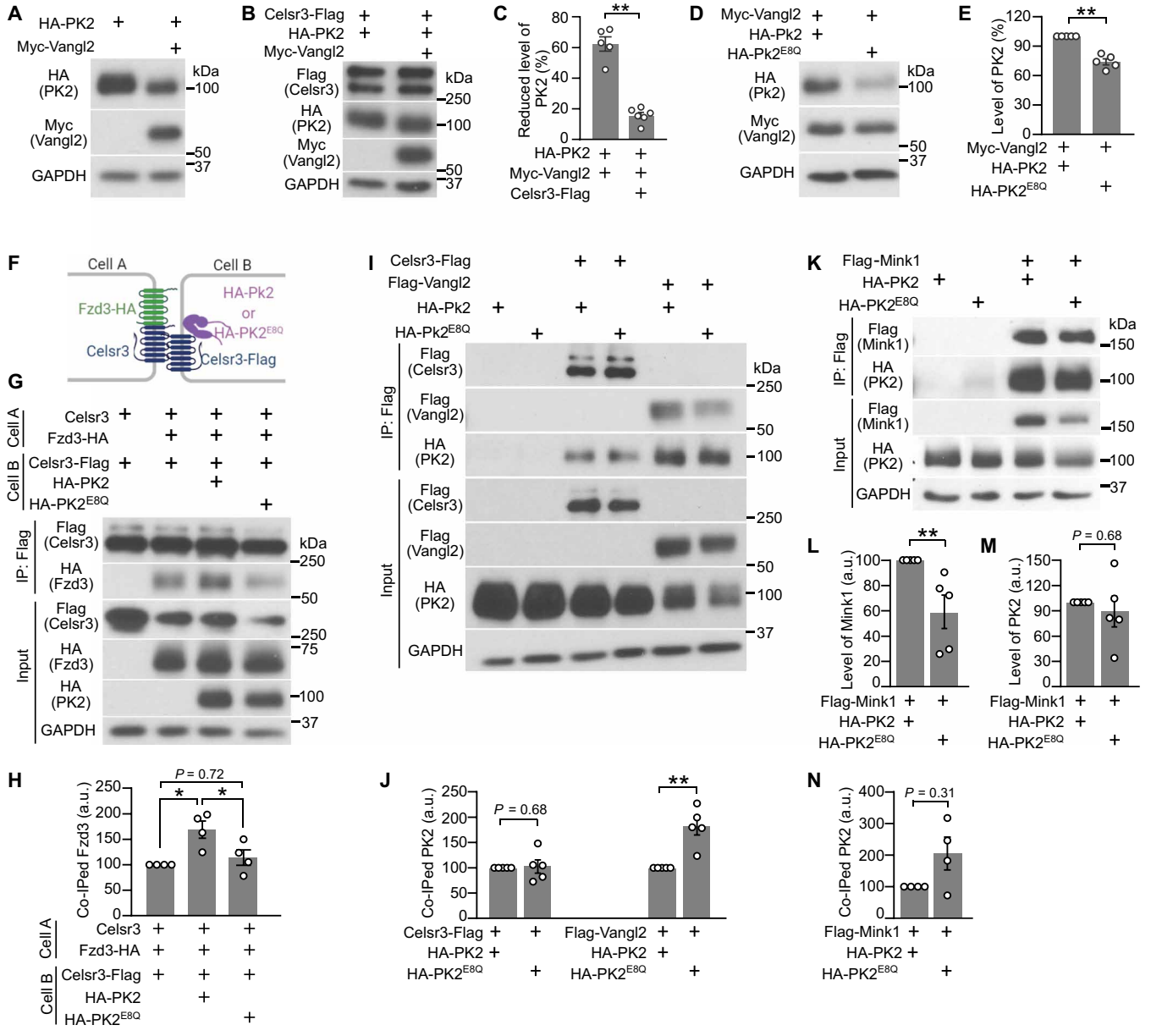

Fig. 6. PK2^{E8Q} is unstable and unable to stabilize the Celsr3/Fzd3-Celsr3 intercellular complex. (**A** to **C**) Regulation of PK2 protein stability by Vangl2 and Celsr3. Cotransfection with Myc-Vangl2 caused a reduction in the level of HA-PK2 in HEK293T cells (A). Myc-Vangl2 could not lead to reduced level of HA-PK2 when Celsr3-Flag was coexpressed (B). Percentage of the reduced level of HA-PK2 from (A) and (B) was plotted in (C). (**D** and **E**) The stability of PK2 E8Q mutant protein. For quantification shown in (C) and (E), each data point represents one independent experiment, Mann-Whitney *U* test, $^{**}P < 0.01$. (**F** to **H**) The stability of the Celsr3/Fzd3-Celsr3 intercellular complex by WT PK2 and PK2 E8Q. Each data point represents one independent experiment, one-way ANOVA, $^{*}P < 0.05$. (**I** and **J**) Co-IP to test the interaction between Vangl2 and PK2 E8Q or between Celsr3 and PK2 E8Q. (**K**) Co-IP to test the interaction between Mink1 and PK2 E8Q. (**L** and **M**) Quantification of the level of Mink1 and PK2 in the input sample shown in (K). (**N**) Quantification of coIPed HA(PK2) with anti-Flag shown in (K). Each data point from (J) and (L) to (M) represents one independent experiment, Mann-Whitney *U* test, $^{**}P < 0.01$. Data shown in (E), (H), (J), and (L) to (N) were normalized by dividing each value to the value of the control group in each independent experiment. Error bars represent SEM.

highlighting the active role of PCP signaling in glutamatergic synapse assembly and maintenance (Fig. 7). We also discerned a hierarchical interaction between PK2 and Vangl2 such that Vangl2 promotes the interaction between PK2 and Celsr3, a complex that promotes synapse formation, but PK2 reduces the interaction between Vangl2 and Celsr3, a complex that reduces synapse formation (Fig. 5). This interaction suggests that PK2 may be the dominating signal to stabilize the intercellular PCP complex (Celsr3/Fzd3-Celsr3) and promote synapse formation.

To understand the more precise roles of PKs in synapse formation and maintenance, our *PK* knockouts were carried out either at P7 or in adulthood. It is important to knock out *PKs* postnatally to test their functions in synapse formation and maintenance, because PCP signaling is important for the guidance of many classes of

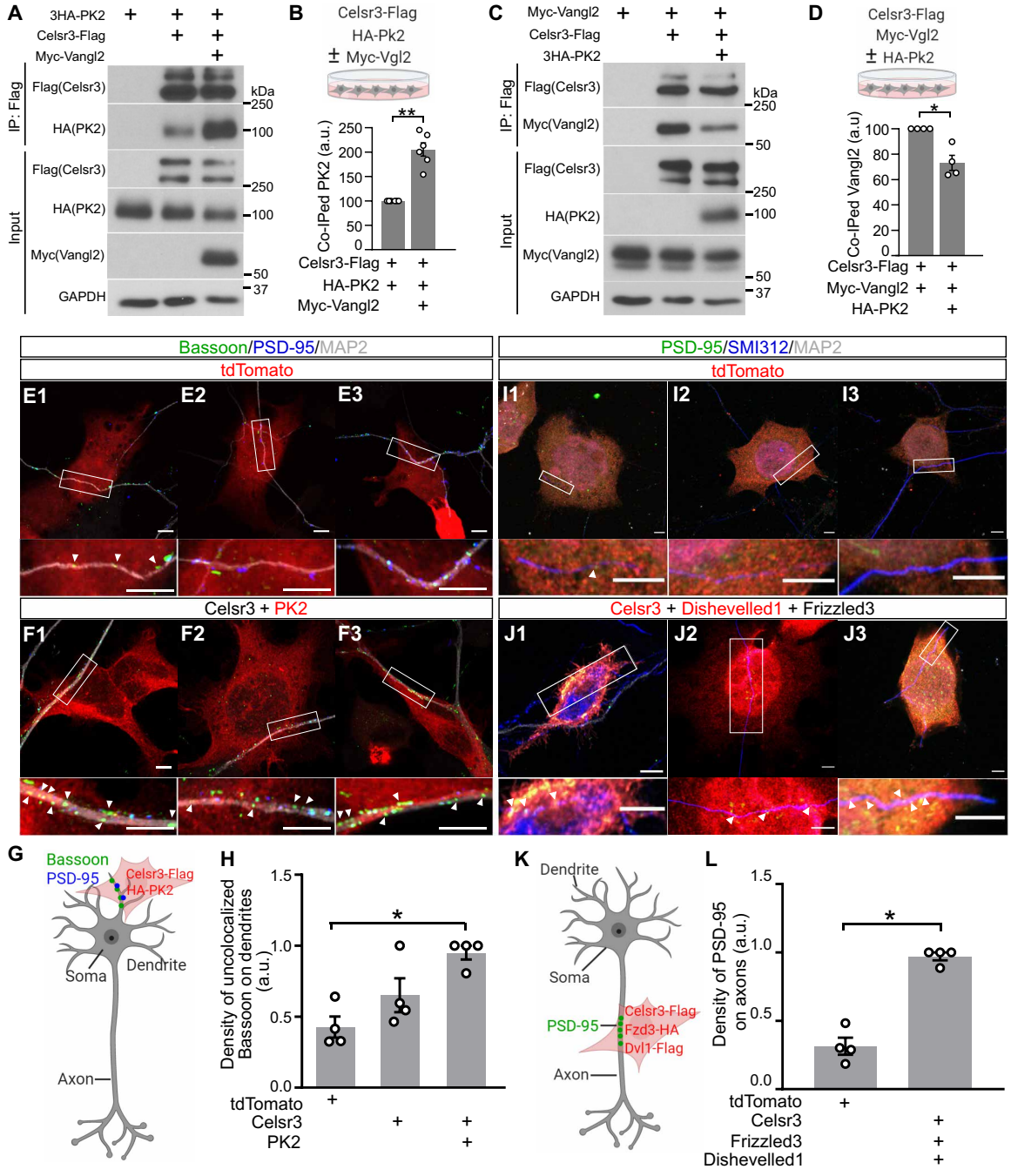

Fig. 7. PCP proteins specify the presynaptic and postsynaptic polarity. (**A** and **B**) The effect of Vangl2 on the interaction between PK2 and Celsr3. (**C** and **D**) The effect PK2 on the interaction between Vangl2 and Celsr3. Each data point in (B) and (D) represents one independent experiment. Data were normalized by dividing each value to the value of the first group in each independent experiment. Mann-Whitney *U* test, $^{*}P < 0.05$ and $^{**}P < 0.01$. (**E** to **H**) Accumulation of the presynaptic marker, Bassoon, on the dendrites of primary hippocampal neurons contacting HEK293T cells expressing Celsr3 and PK2. Scale bars, 5 μm. Each data point represents one independent experiment. Eight to 10 images were analyzed in each experiment. Kruskal-Wallis test was used to compare the means of three groups, and Dunn's test was used to perform multiple comparisons, $^{*}P < 0.05$. (**I** to **L**) Accumulation of the postsynaptic marker, PSD-95, on the axons of primary hippocampal neurons contacting HEK293T cells expression Celsr3, Fzd3 and Dvl1. Scale bars, 5 μm. Each data point represents one independent experiment. Eight to 10 images were analyzed in each experiment. Data were normalized by dividing each value to the maximum value in each independent experiment. Mann-Whitney test, $^{*}P < 0.05$. Error bars represent SEM.

axons (*31*–*33*). Germline knockout *PKs* or knocking out *PKs* at embryonic stage may lead to axon guidance defects, which may secondarily influence synapse formation, complicating the conclusion about their roles in synapse formation. The function of Vangl2 in destabilizing PK2 and increasing N-cadherin endocytosis would both be consistent with its function in reducing synapse formation in development and reducing synapse numbers in adulthood (*35*). However, in a Vangl2 mutation, *looptail*, synapse number was

found reduced in vivo (*35*). This is likely because the severe early phenotypes of *looptail*, including open neural tube and defects of axon guidance, may have a secondary effect on synapse formation (*36*, *37*). Similarly, *Celsr3* was conditionally knocked out using the Foxg1-Cre or Dlx-Cre, which express Cre in early development, and earlier defects, such as altered hippocampal architecture, massive axon projection defects, and reduced branches and lengths of dendrites, were observed (*38*). Glutamatergic synapse numbers were found reduced, and the proportion of inhibitory synapse was found increased (*38*). When Celsr3 was conditionally knocked out postnatally, only glutamatergic synapse numbers were decreased, without these earlier developmental defects (*14*).

The PK protein level is known to be actively regulated by the ubiquitin proteosome degradation pathway. Vangl2 was shown to promote PK2 degradation (*30*). We show here that this function of Vangl2 is inhibited by Celsr3 (Fig. 6), providing additional mechanistic insights of the opposing functions of Celsr3 and Vangl2 in regulating synapse formation and maintenance (*14*). By analyzing a PK2 point mutation found in human patients of autism, we observed that the E8Q mutation renders PK2 protein to be more unstable, potentially due to its increased interaction with Vangl2 protein (Fig. 6). The mutant PK2 protein fails to antagonize Vangl2 and stabilize the aforementioned intercellular PCP complex. We generated a mouse line carrying the *PK2 E8Q* mutation and found that the mutant PK2 protein is less abundant in the PSD, whereas Vangl2 is more abundant in the PSD in vivo (Fig. 4). We characterized the changes of the compositions of synaptic proteins in the *PK2 E8Q* mice in vivo and found that, in addition to the changes of PCP proteins, decreased mutant PK2 protein, and increased Vangl2, several key synaptic proteins were reduced. Those include the glutamate receptors and the MAGUK proteins (Fig. 4). These results provide a clue that PKs may be one of the PCP components that may regulate the composition of the key synaptic proteins, allowing further studies for mechanisms of how PCP signaling regulates the formation and maintenance of the glutamatergic synapses in the future. The *PK2 E8Q* mice are also a valuable tool to study diseases related to synapse formation, stability, and function in autism (*15*). One of the PK-interacting proteins we found reduced in the synaptosome fraction in the *PK2 E8Q* mice was Mink1, which is associated with Alzheimer's disease, Alzheimer's Disease 15, suggesting that the reduction of Mink1 protein level in these patients with Alzheimer's disease may lead to reduced synapse stability due to the reduced PK function (*39*–*42*). Consistent with this, we found that the PCP components are a direct target of amyloid β oligomer–induced synapse degeneration in a mouse model of Alzheimer's disease (in press at *Science Advances*).

MATERIALS AND METHODS

Mice

All experiments were conducted in accordance with the National Institutes of Health Guide for the Care and Use of Laboratory Animals approved by the University of California San Diego (UCSD) Animal Subjects Committee (approved protocol no. S06219). Mice were housed on a 12-hour light/12-hour dark cycle (7 a.m. to 7 p.m.) with rodent chow and water ad libitum. C57BL/6J (stock no. 000664) and Cre-dependent Cas9 knock-in mice (stock no. 026175) were obtained from the Jackson Laboratory. *PK2 E8Q*, *PK1* cKO, and *PK2* cKO mice were generated in the laboratory using the CRISPR-Cas9 system. These *PK1* and *PK2* mutant lines were backcrossed onto the C57BL/6J greater than seven generations for the analyses and quantification of the phenotypes.

Generation of the PK2 E8Q, PK1 cKO, and PK2 cKO mice

Guide RNAs (gRNAs) were designed using the online CRISPR tool (http://tools.genome-engineering.org) and tested in the N2A cell line before in vivo injections (*43*). The CRISPR mix containing the Cas9 protein, sgRNAs, and the single-stranded oligo donor (ssODN) repair templates was injected into 0.5-day C57BL6 embryo pronucleus. On the same afternoon, injected embryos were implanted into the fallopian tube of recipient ICR females, and pups were born 21 days after implantation. The embryo microinjection was carried out in the UCSD transgenic core.

For the *PK2 E8Q* mice (Fig. 3, A to C), the sgRNA sequence is TCAAACTCTTGTCCAGAGCT. The ssODN is TTTGAGCGAAGAAGAGAAGAAGGAGCTGCAGGTGTTCAGTG CTCAGCAAAAGAAAGAAGCTCTGGGGAGAGGAACTATTAAGTTGTTGTCCAGAGCTGTGATGCACGCCGTGTGTGAGCAGGTAGGCCCTCTCTAGAGCGAGCAGAGGGTTGGTGGGAGC.

The loxP insertion sites in the *PK1* cKO mice were located in intron 1 and intron 2, flanking exon2, where the start codon of *PK1* is located (Fig. 2A). The sgRNA sequence for intron 1 is CTAATTGCCTGAG TGGCACG. Sequence of ssODN for intron 1 is GTTTTCTTTGGTACTGAGCTGGTTAAGGGAGTCACTTCCTAATTGCCTGAGTGGCACTAGTATAACTTCGTATAATGTATGCTATACGAAGTTATACGGGGCCTGAAGTCAGCAAACCCAGGCGTTTGGTTCACTGTCTCTGAGCCCATC. sgRNA sequence for intron 2 is TGCATTTGCATTAATCACGA. ssODN sequence for intron 2 is GGCTTTGCTGTCTAAGGTCTGGTTTGGTTTCAGTAATGCCCTCCTTCTGCCATCGGGTACCATAACTTCGTATAATGTATGCTATACGAAGTTATTGATTAATGCAAATGCAGGGCACCACAGGCGTTTCTGATAGGACTTTCACAAGTC.

For the *PK2* cKO allele, we took a similar strategy as the *PK 1* cKO allele described above. The two loxP sequences were inserted in intron 1 and intron 2 flanking exon2 containing the start codon of PK2 (Fig. 2B). sgRNA sequence targeting intron 1 is GACATAATACACGTGCCATA. ssODN sequencing for intron 1 is TGAGTTAGCACACTCACCTGGTAGTTCCTGATCATCACCTAAGTGGCTTCCATATACTAGTATAACTTCGTATAATGTATGCTATACGAAGTTATGGCACGTGTATTATGTCTTTTGTAAACCAGTGCTCTCTAGATTGTAGCTGGTGAC. sgRNA sequence targeting intron 2 is TCAGGGTTGTG TGGCAATAA. ssODN sequence for intron 2 is CATACCCCAGC TTAGAAGGGAAAGGTGGCTCTGCTGACTCAGGGTTGTGTGGCAAGGTACCATAACTTCGTATAATGTATGCTATACGAAGTTATTAAAGGAGTTAAAGATATTCTAGGCCCCGATGGGAAATGGAGCCAAGCCTAGAAT.

Genotyping

Genotyping of all animals was done by PCR using genomic DNA prepared from the tails. Tail lysates were prepared by immersing 0.5-cm tail pieces in 300 μl of 50 mM NaOH solution, incubating for 1 hour at 95°C to lyse the tissues. Tail lysates were mixed with 30 μl of 1 M tris (pH 8) by vortexing and then centrifuging at 12,000*g* for 2 min. The supernatants were used as DNA templates for PCR (Apex Taq RED 2X Master Mix, Genesee Scientific; 42138).

For the *PK2 E8Q* mice, the WT allele was genotyped using primers 5′-GTAACAGTGATGCCGCTGGAG-3′ and 5′-CTTTCCTAATGCTG CAACCCAC-3′. The mutant allele was genotyped using primers 5′-CATGGTAACAGTCATGCCATTACAA-3′ and 5′-CTTTCCTAATGCTGCAACCCAC-3′. The PCR products for WT and mutant alleles are 647 and 651 base pairs (bp), respectively (Fig. 3, B and C).

To confirm the *PK1* cKO allele, we designed the PCR primers, 5′-AGGGATAACACTCTCGGCTG-3′ (P1) and 5′-GCCAGGACTACACAGTGAGACC-3′ (P2). The PCR products were then analyzed by Spe I and Kpn I digestion (1003 bp). The three DNA fragments, 302, 480, and 221 bp, confirmed that the two LoxP sites were inserted in cis (fig. S4A). For routine genotyping, PCR was done using primers designed to amplify the LoxP sequence located at intron 1 (P3, 5′-TTAAAGGCAACAGAGAGCACTAGC-3′; P4, 5′-GGGTGACATAGAAGGCGCTG-3′) and the loxP site located at intron 2 (P5, 5′-CCGAGCAGGTAGGTAGGAAG-3′; P6, 5′-CCTATCAGAAACGCCTGTGG-3′). The PCR products are 251 and 217 bp, respectively (fig. S4A).

To confirm the *PK2* cKO allele, we designed the PCR primers, 5′-GGGAATTGTGGTCATGGTTC-3′ (P1) and 5′-CATGTTGGTGCTCTGATGCT-3′ (P2). The PCR product (909 bp) was digested then by Spe I and Kpn I. The three DNA fragments (174, 507, and 228 bp) confirmed that the two LoxP sites were inserted in cis (fig. S4B). For routine genotyping, PCR was done using primers designed to amplify the loxP sequence located at intron 1 (P3, 5′-TTGGAAGAAGGTTGGGTTTG-3′; P4, 5′-TACTTGCCAGTCACCGTCCT-3′) and the loxP site at intron 2 (P5, 5′-CCCAGCTTAGAAGGGAAAGG-3′; P6, 5′-CTGCGCTCCAAAACATAACA-3′). The PCR products are 211 and 249 bp, respectively (fig. S4B).

cDNA, sgRNA constructs, and virus generation

The Celsr3-Flag, Celsr3–internal ribosomal entry site–GFP, Myc-Vangl2, Flag-Vangl2, and Fzd3-HA constructs used for the biochemical studies in the HEK293T cell and in the hippocampal neuron/HEK293T mixed culture experiments were previously generated and characterized in Zou laboratory (*28*, *37*). WT mouse PK2 and $PK2^{E8Q}$ was cloned into pcDNA 3.1 expression vector with 3XHA tag attached to its N terminus by VectorBuilder. Sequences of sgRNAs are as follows: *PK2* sgRNA1 (5′-ACAGCCAGAGTCGTCATCTG-3′), *PK2* sgRNA2 (5’-CAGAGGAAACGTGAGAACCT-3′), *PK1* sgRNA1 (5′-GTTGCCTCCACACGATAACG-3′), *PK1* sgRNA2 (5′-GAGGTAAAGCCGAATCACCA-3′), and control sgRNA (5′-TGCGAATACGCCCACGCGAT-3′) (*19*, *44*, *45*). All *PK1* and *PK2* sgRNA were first tested in the N2A cell line by inserting annealed complementary oligonucleotide into psPCas9 (sgRNA) backbone. For in vivo experiments, complementary oligonucleotides were annealed and inserted into AAV: ITR-U6-sgRNA-hSyn-Cre backbone (*19*). All constructs were verified by sequencing (Eton Biosciences).

AAV was produced by transfection of AAV293 cells with three plasmids: an AAV vector expressing target constructs (U6-sgRNA-hSyn-Cre), AAV helper plasmid, and AAV rep-cap helper plasmid (a gift from B. Lim at UCSD). Seventy-two hours after transfection, cells were harvested and lysed. Viral particles were purified by an iodixanol step-gradient ultracentrifugation method. The iodixanol was diluted, and the AAV was concentrated using a 100-kDa molecular mass cutoff ultrafiltration device. The genomic titer was determined by quantitative real-time PCR (*46*).

Cell line, transfection, and coimmunoprecipitation

The HEK293T cell line (RRID: CVCL_0063) was purchased from American Type Culture Collection (ATCC) and maintained in Dulbecco’s modified Eagle’s medium (Thermo Fisher Scientific, 10-017-CV) containing 10% fetal bovine serum (Thermo Fisher Scientific, 10439024) and 1% penicillin-streptomycin (Thermo Fisher Scientific, 15140122). Transfection was carried out by incubating the cells with a mixture containing 1:3 ratio of plasmid DNA to polyethyleneimine MAX (Polyscience, 24765). Forty-eight hours after transfection, HEK293T cells were lysed with lysis buffer [20 mM tris (pH 7.5), 150 mM NaCl, 2 mM EGTA, 0.1% Triton X-100, and protease and phosphatase inhibitor (Thermo Fisher Scientific, 78441)]. Lysates were immunoprecipitated with anti-Flag antibody (Millipore Sigma, F7425) and with Protein A/G plus agarose (Santa Cruz Biotechnology, sc-2003).

Synaptosome extraction

The synaptosome fraction (P2) was extracted as described previously (*14*, *47*). Briefly, cortex and HPC from P14 mice were homogenized to 10% (w/v) in ice-cold 0.32 M sucrose buffer containing 1 mM $MgCl_2$, 0.5 mM $CaCl_2$, 1 mM $NaHCO_3$, and protease/phosphatase inhibitors (Thermo Fisher Scientific, 78441) using 16 strokes with a glass dounce. The homogenate was spun at 710*g* for 30 min at 4°C to pellet out nuclei and large debris. The supernatant was further centrifuged at 13,800*g* for 10 min at 4°C to get the P2 pellets, which were resuspended in the sucrose buffer and stored at −80°C for future use.

PSD preparation for mass spectrometry

PSD fractions were prepared from mouse cortex of P21 mice as described (fig. S1B) (*48*). All centrifugation steps were performed at 4°C. Protease inhibitors (Thermo Fisher Scientific, 87785) and phosphatase inhibitors (Roche Diagnostics, 04906837001) were added into all buffers. Mice cortex was homogenized in ice-cold buffer A [5 mM Hepes (pH 7.4), 1 mM $MgCl_2$, and 0.5 mM $CaCl_2$] using 12 strokes with a glass dounce. The homogenate was spun at 1400*g* for 10 min. The supernatant (S1) was saved, and pellet (P1) was homogenized again with buffer A for five strokes and then centrifuged at 700*g* for 10 min. The supernatant (S1′) was pooled with S1 and centrifuged at 13,800*g* for 10 min for collect the pellet (P2). P2 collected from the cortex of two animals with the same genotype was pooled together, resuspended in buffer B [0.32 M sucrose and 6 mM tris (pH 8.0)], homogenized for five strokes, and was loaded onto a discontinuous sucrose gradient [0.85/1/1.15 M sucrose solution in 6 mM tris (pH 8.0)], followed by centrifugation at 82,500*g* for 2 hours. The synaptosome fraction between 1 and 1.15 M sucrose was collected and mixed with equal volume of buffer C [6 mM tris (pH 8.1) and 1% Triton X-100] for 15 min at 4°C under agitation. The mixture was spun at 32,800*g* for 20 min. The resulting pellet (PSD I) was resuspended in buffer D [6 mM tris (pH 8.1) and 0.5% Triton X-100] for 15 min at 4°C under agitation and then spun at 201,800*g* for 1 hour. The pellet (PSD II) was used for mass spectrometry analysis.

The PSDII pellet was digested according to the previously described method (*49*). Samples diluted in TNE buffer [50 mM tris (pH 8.0), 100 mM NaCl, and 1 mM EDTA] with 0.1% RapiGest SF were boiled for 5 min, then mixed with 1 mM tris (2-carboxyethyl) phosphine (TCEP), and incubated at 37°C for 30 min. Next, the samples were carboxymethylated with iodoacetamide (0.5 mg/ml)

for 30 min at 37°C and neutralized with 2 mM TCEP followed by trypsin digestion overnight at 37°C. Then, samples were treated by 250 mM HCl at 37°C for 1 hour and centrifugation at 14,000 rpm for 30 min at 4°C to remove RapiGest. Peptides in the soluble fraction were extracted and desalted using C18 desalting columns (Thermo Fisher Scientific, PI-87782) and quantified using bicinchoninic acid (BCA) protein assay. One microgram of peptides was injected for liquid chromatography–mass spectrometry analysis at the UCSD core facility. Three independent experiments were conducted.

Western blot

Denatured protein samples were loaded and electrophoresis on 8% SDS–polyacrylamide gel electrophoresis gels (homemade). Proteins were then transferred onto an Immobilon-P polyvinylidene difluoride membrane (Millipore Sigma; IPVH00010), blocked with 5% nonfat dry milk in TBST (0.05% Tween-20 in tris-buffered saline) and incubated with primary antibodies diluted in blocking buffer overnight at 4°C. Membranes were washed three times in TBST for 10 min each and incubated with secondary antibodies for 1 hour at room temperature followed by a similar wash step. Bands were detected by incubating the membrane with WestPico chemiluminescent substrate (Thermo Fisher Scientific, 34580) and documented with an x-ray film (Thermo Fisher Scientific, 34091).

Primary antibodies used for Western blot analysis include anti-Flag (Millipore Sigma, F7425), anti-HA (BioLegend, 901513), anti-Myc (Santa Cruz Biotechnology, sc-40), anti–glyceraldehyde-3-phosphate dehydrogenase (Millipore Sigma, MAB374), anti–β-actin (Abcam, ab8227), anti-Celsr3 (customized), anti-PK1 (Proteintech, 22589-1-AP), anti-PK2 (Millipore Sigma, MABN1529), anti-Vangl2 (R&D Systems, AF4815), anti-GluR1 (Millipore Sigma, MAB2263), anti-GluR2 (Thermo Fisher Scientific, 320300), anti-NR1 (Neuromab, 75-272), anti-NR2A (Millipore Sigma, 07-632), anti-NR2B (BioLegend, 832501), anti–PSD-95 (Abcam, ab12093), anti–PSD-93 (Millipore Sigma, MABN497), anti–SAP97 (Antibodies Incorporated, 75-030), anti–SAP102 (Antibodies Incorporated, 75-058), anti-Mink1 (Thermo Fisher Scientific, PA5-28901), anti-synaptic vesicle 2 (SV2) (Developmental Studies Hybridoma Bank), and anti–CRISPR-Cas9 (Abcam, ab191468).

Hippocampal neuron and HEK293T coculture

The mixed culture assay was performed as described with modifications (*27*). Dissociated hippocampal neurons were prepared from embryonic day 18 (E18) mouse hippocampi and cultured in Neurobasal medium (Thermo Fisher Scientific, 21103049) supplemented with B27 (Thermo Fisher Scientific, 17504044), GlutaMAX (Thermo Fisher Scientific, 35050061), and penicillin-streptomycin (Thermo Fisher Scientific, 15140122) on glass coverslips (12 mm) coated with poly-D-lysine (Millipore Sigma, P6407). Neurons were plated at 300,000 per well in six-well plates and were maintained in a humidified 37°C incubator with 5% CO_2. To test the role of PCP signaling in synapse formation, at 7 days in vitro (DIV7) of the neuronal culture, HEK293T cells were transfected with indicated plasmids. Forty-eight hours after transfection (DIV9), HEK293T cells were fully dissociated and seeded atop the dissociated hippocampal neurons. At DIV11, mixed culture was fixed and stained. The next day, samples were incubated with secondary antibodies and mounted with Fluoromount-G for imaging. Images were taken using the fast airyscan mode of Zeiss LSM880 microscopy. To test whether PK2 and Celsr3 promote the accumulation of presynaptic marker on dendrites, transfected HEK293T cells were cocultured with hippocampal neurons at DIV10 to DIV12. To test whether Celsr3, Fzd3, and Dvl1 can induce the accumulation of postsynaptic markers on axons, transfected HEK293T cells were cocultured with hippocampal neurons at DIV12 to DIV14. Primary antibodies used in the coculture assay include anti-Flag (Millipore Sigma, F7425), anti-HA (Abcam, ab9110), anti-microtubule-associated protein 2 (MAP2) (Abcam, ab5392), anti-neurofilament marker (BioLegend, 837904), anti-Bassoon (Synaptic Systems, 141004), and anti–PSD-95 (Millipore Sigma, MAB1596).

Stereotaxic viral injections

Adult mice (8 to 9 weeks old) were anesthetized by intraperitoneal injection with a mixture of ketamine (100 mg/kg) and xylazine (10 mg/kg). Pups (7 to 8 days old) were anesthetized by inhalation with 2.5% isoflurane and oxygen. Individual mouse was mounted in a stereotaxic frame. Body temperature was kept stable by using a heating pad during surgery and recovery. For synapse quantification, AAV-U6-sgRNA-hSyn-Cre virus in volumes of 150 to 300 nl was injected bilaterally into the dorsal HPC [adults: bregma, anteroposterior (AP) −2.0 mm; lateral (L) ±1.5 mm; dorsoventral (DV) −1.7, −1.9, and −2.1 mm; pups: lambda, AP +1.6 mm; L ± 1.5 mm; DV −2.2 and −2.4 mm)] and medial prefrontal cortex (mPFC) (adults: bregma, AP +2.0 mm; L ±0.3 mm; DV −1.9 and −2.1 mm; pups: lambda, AP +3.6 mm; L ±0.3 mm; DV −1.8 and −2.0 mm) of cre-dependent cas9 mice at a slow rate (30 to 50 nl/min) using a glass pipette connecting to a syringe pump. Mouse brains were harvested 2 to 4 weeks after virus injection for immunostaining. All injection sites were verified during imaging. Animals with incorrect injections were excluded from analysis. For dendritic spine labeling, 100 nl of AAV1-hSyn-Cre-eGFP and AAV1-CAG-Flex-eGFP virus mixture (1:5000) was injected bilaterally into the CA1 (adults: bregma, AP −2.0 mm; L ± 1.5 mm; DV −1.8 mm; pups: lambda, AP +1.6 mm; L ±1.5 mm; DV −2.2 mm) and mPFC (adults: bregma, AP +2.0 mm; L ±0.3 mm; DV −1.9 mm; pups: lambda, AP +3.6 mm; L ±0.3 mm; DV −1.8 mm) of PK1 flox/flox, PK2 flox/flox mice, and their WT littermates. Mouse brains were collected and sectioned 2 to 4 weeks after virus injection.

Immunohistochemistry and immunocytochemistry

Immunohistochemistry was performed according to the previously described method (*14*). Briefly, mice were perfused with phosphate-buffered saline (PBS) and 4% paraformaldehyde (PFA) at P14. Brains were removed and postfixed in 4% PFA overnight at 4°C. Brains were cryoprotected by immersing in 30% sucrose until the tissue sink to the bottom. Brains were then embedded in optimal cutting temperature (OCT) compound and 30% sucrose mixture (1:1) and frozen on dry ice. Coronal free-floating sections (4 μm thick) were collected, treated with 1% SDS for antigen retrieval, and used for immunostaining. Primary antibodies used for immunohistochemistry include anti-Bassoon (Synaptic Systems, 141004), anti–PSD-95 (Abcam, ab12093), anti-GFP (Abcam, ab6556-25), anti-PK2 (BiCell Scientific, 50622), anti-Vangl2 (Santa Cruz Biotechnology, sc-515187), and anti-CC3 (ASP175) (Cell Signaling Technology, 9661). Fluorescent image stacks (20 images per Z stack, size of each image: 73.88 μm by 73.88 μm) were acquired using a Zeiss LSM510 or Leica SP8 confocal microscope with a 63× oil-immersion lens and 2.5× zoom. The number of synaptic puncta was analyzed using ImageJ's synapse counter plugin (*50*). The number and average size of PK2 and Vangl2 puncta were achieved by using the analyze particle

command in ImageJ. Experimenters who took fluorescent images and quantified the number of synapses were blinded to the treatments of animals.

HEK293T cells were grown on poly-D-lysin–treated (Millipore Sigma, P6407) coverslips and transfected as described above. Forty-eight hours after transfection, cells were fixed in 4% PFA for 15 min, permeabilized with 0.2% Triton X-100 in PBS for 10 min, and blocked with a 3% normal donkey serum (NDS) in PBS for 2 hours at room temperature. Cells were immunostained with rabbit anti-Flag (Millipore Sigma, F7425) and mouse anti-HA (BioLegend, 901513) antibodies in 3% NDS overnight at 4°C and subsequently labeled with secondary antibodies. Coverslips were mounted onto slides using Fluoromount-G (SouthernBiotech, 0100-01). Images of samples were acquired with a Zeiss LSM 880 microscopy with a 63× oil-immersion lens.

Sequential immunohistochemistry

Mouse brain sections were sequentially immunolabeled with goat anti–PSD-95, rabbit anti-PK1, and rabbit anti-PK2. On day 1, free-floating mouse brain sections were treated with 1% SDS for antigen retrieval, then washed twice with PBS (10 min each), and blocked with NDS for 1 hour at room temperature. After blocking, tissue was washed three times with PBS (20 min each) and incubated with goat anti–PSD-95 (Abcam, ab12093) overnight at 4°C. On day 2, tissue was washed in similar fashion with PBS and incubated with Alexa 568–conjugated donkey anti-goat antibody for 2 hours at room temperature. After incubation, tissue was washed and incubated with Rabbit anti-PK1 (BiCell Scientific, 50621) overnight at 4°C. On day 3, tissue was washed and incubated with Alexa 647–conjugated Donkey anti-rabbit antibody for 2 hours at room temperature. After incubation with the second secondary antibody, tissue was washed and incubated with normal rabbit serum. The purpose of this step was to saturate open binding sites on the second secondary antibody with immunoglobulin G (IgG) so that they could not capture the third secondary antibody. We then washed the tissue and incubated them with an excess amount of AffiniPure Fab Fragment Donkey Anti-Rabbit IgG (H+L) (Jackson ImmunoResearch, 711-007-003) for 2 hours at room temperature. After incubation, tissue was washed and incubated with the third primary antibody, rabbit anti-PK2 (BiCell Scientific, 50622), overnight at 4°C. On day 4, tissue was washed and incubated with Alexa 488–conjugated donkey anti-rabbit antibody for 2 hours at room temperature. Tissue was washed and mounted in Fluoromount-G (SouthernBiotech, 0100-01) for imaging.

Sample preparation for 3D-STORM

P14 and adult mouse brains were collected, fixed, and cryoprotected as described above. Frozen brain sections (10-μm-thick) were quenched with 20 mM glycine in Dulbecco's PBS (DPBS; Thermo Fisher Scientific, 14040133) for 5 min, followed by permeabilization and blocking with 10% donkey serum and 0.3% Triton X-100 in DPBS for 1 hour at room temperature. Tissues were then incubated with primary antibodies including goat anti–PSD-95 (Abcam, 12093), Guinea pig anti-Bassoon (Synaptic Systems, 141004), and rabbit anti-PK1 (BiCell Scientific, 50621) or rabbit anti-PK2 (BiCell Scientific, 50622) overnight at 4°C and secondary antibodies including donkey anti-goat IgG (H+L) Alexa Fluor 568 (Thermo Fisher Scientific, A-11057), donkey anti–Guinea pig IgG (H+L) Alexa Fluor 647 (Jackson ImmunoReseach, 706-605-148), and donkey anti-rabbit IgG (H+L) Alexa Fluor 488 (Jackson ImmunoResearch, 711-545-152) for 1 hour at room temperature. After antibody incubation, brain sections were fixed in 3% PFA with 0.05% glutaraldehyde (Millipore Sigma, G7526) for 5 min and mounted on glass coverslips (Thermo Fisher Scientific, 125485M). Immediately before imaging, brain sections mounted on glass coverslips were wettened using 100 μl of freshly prepared STORM buffer [50 mM tris (pH 8.0), 10 mM NaCl, 10% glucose, 0.1 M mercaptoethanolamine, glucose oxidase (56 U/ml), and catalase (340 U/ml)] and sealed using nail polish.

3D STORM imaging and analysis

The STORM technology used for the present study has been developed by the Xiaowei Zhuang laboratory at Harvard University and licensed to Nikon (*16*). Imaging and analysis were performed as described previously (*51*). Image acquisition was performed on a Nikon A1R Confocal STORM superresolution system with a 100×/1.49 TIRF oil-immersion objective and an ANDOR IXON3 Ultra DU897 EMCCD camera in multicolor mode set by the Nikon NIS-Elements AR 5.21.01 software. The position of individual molecules was localized by switching them on and off sequentially using the 488-, 568-, and 647-nm lasers at appropriate power settings. The error was considerably reduced by calculating and correcting for sample drift during the experiment by an autocorrelation method implemented by the Nikon software. Axial drift over the course of the acquisition was minimized by engaging the Nikon perfect focus system. Images obtained on the Nikon N-Storm system were converted to high-resolution images, fully calibrated, and imported into Nikon NIS-Elements analyzer for visualization.

Dendritic spine density analysis

Individual neurons and their dendrites were sparsely labeled by GFP after injection with diluted AAV1-hSyn-Cre (1:5000) mixed with AAV1-CAG-Flex-eGFP virus. Two to 4 weeks after virus injection, mice were perfused with 4% PFA. Forty-micrometer-thick coronal free-floating sections were collected as described above. Sections were stained with 4′,6-diamidino-2-phenylindole and mounted in Fluoromount-G. In HPC, we focused on oblique apical dendrites of CA1 pyramidal neurons. These spines represented the postsynaptic structures of the Schaffer collateral-CA1 synapses. In mPFC, we imaged the distal dendrites of pyramidal neurons. Images were taken using the superresolution mode of Zeiss LSM 880 microscopy with Airyscan. Dendritic segments and spines were reconstructed in 3D from image stacks and detected automatically with Imaris (Oxford Instruments). Protrusions with head diameter > 0.1 μm and length < 5 μm were detected for analysis. Experimenters who took fluorescent images and analyzed spines were blinded to the genotypes of animals.

Behavioral assays

All behavioral tests were performed on mice 2 to 3 months of age. Mice were weaned at P21 and housed in groups of two to five of the same gender. They were maintained under a 12-hour light/12-hour dark cycle with ad libitum access to food and water, except during the tests. Both male and female mice were used in these assays. On the test day, all the cages containing test mice were transferred to the behavior testing room 1 hour before the first trial begins. All apparatus were cleaned with 70% (v/v) ethanol between animals. Visual cues were minimized unless they are required. For open field test, light-dark transition test, and Barnes maze test, activities of mice were recorded using a digital high-definition camera (The Imaging

Source) mounted on the ceiling above the apparatus and analyzed using the software Viewer (BIOBSERVE). Littermate controls are used as control group in all tests. Experimenters who performed the behavioral tests and video analysis were blind to the genotypes of tested animals.

Open field test

Mice were placed individually in the center of a plastic open-field arena (40 cm by 40 cm by 34 cm) and allowed to explore freely for 10 min. Experiments were performed during the dark phase of the cycle and under dim light.

Light-dark transition test

The light dark box (40 cm by 40 cm by 34 cm) (Stoelting) was divided into two sections of equal size by a partition with door. The dark compartment was painted black with a closed top, whereas the light compartment is painted white with open top and brightly illuminated (600 lux) with an indirect light source. The door connecting the light and dark compartments was blocked until the individual mouse was placed in the center of the light chamber and allowed to move freely between the two compartments with door open for 10 min. Experiments were performed during the dark phase of the cycle.

Barnes maze test

The Barnes maze apparatus was a customized white circular plexiglass table with a diameter of 90 cm and elevated 56 cm above the ground. Twenty 5-cm-diameter holes were located equidistantly from the perimeter of the table. Four striped geometric shapes (cone, cross, triangle, and circle) were positioned around the maze to use as visual cues and kept constant throughout the test. The escape box is a black Plexiglas box (15 cm long, 6 cm wide, and 6.6 cm high), with a ramp covered with black plastic mesh to allow the animal to easily enter the escape box.

The Barnes maze task was run over the course of 11 days in five phases: habituation (1 day), training (4 days), probe test (1 day), reversal training (4 days), and reversal probe test (1 day). On the habituation day, each animal was placed in the maze next to a hole with escape box. The animal was restrained underneath a clear 2-liter glass beaker and given 5 min to independently enter through the hole into the escape box. If they did not enter on their own, they were guided by the experimenter to enter the escape box and allowed to stay in the escape box for 1 min before being returned to its home cage. The habituation procedure allowed animals to experience the aversive bright light and to practice using the ramp to step down to the escape box.

During the training phase, only the target hold has the escape box underneath, the other 19 holes had "false escapes boxes" (a shallow black box that is 5 cm long, 5 cm wide, and 1.5 cm deep) attached underneath. At the beginning of each training session, individual mouse was placed underneath a start chamber (a black cardboard box) located in the center of the maze for 15 s, which allowed the animal to face a random direction. A buzzer was turned on during this holding period. The trial started when the animal was released from the start chamber. Animals were allowed to explore freely in the maze for 3 min. The trial ended when the mouse entered the escape hole by its own or after 3 min elapsed. If a mouse successfully located the target hold and entered the escape box, then the buzzer was turned off immediately, and the mouse was allowed to stay in the escape box for 1 min before being returned to its home cage. Otherwise, the mouse will be guided into the escape hole when the trial ended. Animals were trained twice a day with 15-min intertrial interval for 4 days. Location of the target hole was kept constant during the training phase and was randomly selected for each animal. The latency to locate the target hole was measured.

For the probe test on day 6, the escape box was removed, and all of the 20 holes were attached to false escape boxes. Animals were released from the start chamber and allowed to freely explore the maze for 3 min with the buzzer turned on. For the analysis, the maze was divided into four quadrants. The target quadrant consisted five holes with the target hole in the center. The other quadrants going clockwise from the target quadrant were right, opposite, and left. The time animals spent in each quadrant was measured.

The reversal training was included to assess the animals' flexibility in changing a previous learned pattern. The procedures were similar to the acquisition training phase, except that the location of the target hole was moved 180° from its location during the acquisition training phase. Memory was assessed on day 11 using the same procedure as the probe test on day 6.

Statistics

All tests are described in the appropriate figure legends. When comparing two groups, data in each group were first assessed by the Shapiro-Wilk normality test. Data were considered to form a normal distribution if the value of the Shapiro-Wilk test was greater than 0.05. Data passed the Shapiro-Wilk test were analyzed by Student's *t* test. Data which did not pass the Shapiro-Wilk test were analyzed with Mann-Whitney *U* test. When comparing more than two groups, data in each group were first assessed by the Shapiro-Wilk normality test. For parametric data, ordinary one-way analysis of variance (ANOVA) was used to compare the means of multiple groups. If significant difference was detected, then the Turkey test was used for multiple comparisons. For nonparametric data, Kruskal-Wallis test was used to compare the means of multiple groups, and Dunn's test was used to perform multiple comparisons. $P < 0.05$ was considered to be a significant difference. All statistical tests were performed using GraphPad Prism software version 9.0.

SUPPLEMENTARY MATERIALS

Supplementary material for this article is available at https://science.org/doi/10.1126/sciadv.abh2974

View/request a protocol for this paper from *Bio-protocol*.

REFERENCES AND NOTES

1. J. C. Watkins, R. H. Evans, Excitatory amino acid transmitters. *Annu. Rev. Pharmacol. Toxicol.* **21**, 165–204 (1981).
2. G. L. Collingridge, S. J. Kehl, H. McLennan, Excitatory amino acids in synaptic transmission in the Schaffer collateral-commissural pathway of the rat hippocampus. *J. Physiol.* **334**, 33–46 (1983).
3. D. T. Monaghan, R. J. Bridges, C. W. Cotman, The excitatory amino acid receptors: Their classes, pharmacology, and distinct properties in the function of the central nervous system. *Annu. Rev. Pharmacol. Toxicol.* **29**, 365–402 (1989).
4. F. Zhu, M. Cizeron, Z. Qiu, R. Benavides-Piccione, M. V. Kopanitsa, N. G. Skene, B. Koniaris, J. DeFelipe, E. Fransén, N. H. Komiyama, S. G. N. Grant, Architecture of the mouse brain synaptome. *Neuron* **99**, 781–799.e10 (2018).
5. M. Cizeron, Z. Qiu, B. Koniaris, R. Gokhale, N. H. Komiyama, E. Fransen, S. G. N. Grant, A brainwide atlas of synapses across the mouse life span. *Science* **369**, 270–275 (2020).
6. M. Sheng, E. Kim, The postsynaptic organization of synapses. *Cold Spring Harb. Perspect. Biol.* **3**, (2011).
7. T. C. Sudhof, The presynaptic active zone. *Neuron* **75**, 11–25 (2012).
8. M. Zagrebelsky, C. Tacke, M. Korte, BDNF signaling during the lifetime of dendritic spines. *Cell Tissue Res.* **382**, 185–199 (2020).
9. D. D. Krueger, L. P. Tuffy, T. Papadopoulos, N. Brose, The role of neurexins and neuroligins in the formation, maturation, and function of vertebrate synapses. *Curr. Opin. Neurobiol.* **22**, 412–422 (2012).

10. H. Y. Kim, J. W. Um, J. Ko, Proper synaptic adhesion signaling in the control of neural circuit architecture and brain function. *Prog. Neurobiol.* **200**, 101983 (2021).
11. F. Varoqueaux, G. Aramuni, R. L. Rawson, R. Mohrmann, M. Missler, K. Gottmann, W. Zhang, T. C. Sudhof, N. Brose, Neuroligins determine synapse maturation and function. *Neuron* **51**, 741–754 (2006).
12. P. T. Kurshan, K. Shen, Synaptogenic pathways. *Curr. Opin. Neurobiol.* **57**, 156–162 (2019).
13. M. T. Butler, J. B. Wallingford, Planar cell polarity in development and disease. *Nat. Rev. Mol. Cell Biol.* **18**, 375–388 (2017).
14. S. Thakar, L. Wang, T. Yu, M. Ye, K. Onishi, J. Scott, J. Qi, C. Fernandes, X. Han, J. R. Yates III, D. K. Berg, Y. Zou, Evidence for opposing roles of Celsr3 and Vangl2 in glutamatergic synapse formation. *Proc. Natl. Acad. Sci. U.S.A.* **114**, E610–E618 (2017).
15. L. P. Sowers, L. Loo, Y. Wu, E. Campbell, J. D. Ulrich, S. Wu, L. Paemka, T. Wassink, K. Meyer, X. Bing, H. El-Shanti, Y. M. Usachev, N. Ueno, J. R. Manak, A. J. Shepherd, P. J. Ferguson, B. W. Darbro, G. B. Richerson, D. P. Mohapatra, J. A. Wemmie, A. G. Bassuk, Disruption of the non-canonical Wnt gene *PRICKLE2* leads to autism-like behaviors with evidence for hippocampal synaptic dysfunction. *Mol. Psychiatry* **18**, 1077–1089 (2013).
16. M. J. Rust, M. Bates, X. Zhuang, Sub-diffraction-limit imaging by stochastic optical reconstruction microscopy (STORM). *Nat. Methods* **3**, 793–796 (2006).
17. B. Huang, W. Wang, M. Bates, X. Zhuang, Three-dimensional super-resolution imaging by stochastic optical reconstruction microscopy. *Science* **319**, 810–813 (2008).
18. A. Dani, B. Huang, J. Bergan, C. Dulac, X. Zhuang, Superresolution imaging of chemical synapses in the brain. *Neuron* **68**, 843–856 (2010).
19. R. J. Platt, S. Chen, Y. Zhou, M. J. Yim, L. Swiech, H. R. Kempton, J. E. Dahlman, O. Parnas, T. M. Eisenhaure, M. Jovanovic, D. B. Graham, S. Jhunjhunwala, M. Heidenreich, R. J. Xavier, R. Langer, D. G. Anderson, N. Hacohen, A. Regev, G. Feng, P. A. Sharp, F. Zhang, CRISPR-Cas9 knockin mice for genome editing and cancer modeling. *Cell* **159**, 440–455 (2014).
20. A. G. Bassuk, R. H. Wallace, A. Buhr, A. R. Buller, Z. Afawi, M. Shimojo, S. Miyata, S. Chen, P. Gonzalez-Alegre, H. L. Griesbach, S. Wu, M. Nashelsky, E. K. Vladar, D. Antic, P. J. Ferguson, S. Cirak, T. Voit, M. P. Scott, J. D. Axelrod, C. Gurnett, A. S. Daoud, S. Kivity, M. Y. Neufeld, A. Mazarib, R. Straussberg, S. Walid, A. D. Korczyn, D. C. Slusarski, S. F. Berkovic, H. I. El-Shanti, A homozygous mutation in human PRICKLE1 causes an autosomal-recessive progressive myoclonus epilepsy-ataxia syndrome. *Am. J. Hum. Genet.* **83**, 572–581 (2008).
21. H. Tao, J. R. Manak, L. Sowers, X. Mei, H. Kiyonari, T. Abe, N. S. Dahdaleh, T. Yang, S. Wu, S. Chen, M. H. Fox, C. Gurnett, T. Montine, T. Bird, L. G. Shaffer, J. A. Rosenfeld, J. McConnell, S. Madan-Khetarpal, E. Berry-Kravis, H. Griesbach, R. P. Saneto, M. P. Scott, D. Antic, J. Reed, R. Boland, S. N. Ehaideb, H. El-Shanti, V. B. Mahajan, P. J. Ferguson, J. D. Axelrod, A. E. Lehesjoki, B. Fritzsch, D. C. Slusarski, J. Wemmie, N. Ueno, A. G. Bassuk, Mutations in prickle orthologs cause seizures in flies, mice, and humans. *Am. J. Hum. Genet.* **88**, 138–149 (2011).
22. M. Mastrangelo, M. Tolve, M. Martinelli, S. P. Di Noia, E. Parrini, V. Leuzzi, PRICKLE1-related early onset epileptic encephalopathy. *Am. J. Med. Genet. A* **176**, 2841–2845 (2018).
23. B. P. Todd, A. G. Bassuk, A de novo mutation in PRICKLE1 associated with myoclonic epilepsy and autism spectrum disorder. *J. Neurogenet.* **32**, 313–315 (2018).
24. H. Algahtani, F. Al-Hakami, M. Al-Shehri, B. Shirah, M. H. Al-Qahtani, A. A. Abdulkareem, M. I. Naseer, A very rare form of autosomal dominant progressive myoclonus epilepsy caused by a novel variant in the PRICKLE1 gene. *Seizure* **69**, 133–139 (2019).
25. Y. Hida, M. Fukaya, A. Hagiwara, M. Deguchi-Tawarada, T. Yoshioka, I. Kitajima, E. Inoue, M. Watanabe, T. Ohtsuka, Prickle2 is localized in the postsynaptic density and interacts with PSD-95 and NMDA receptors in the brain. *J. Biochem.* **149**, 693–700 (2011).
26. A. M. Daulat, O. Luu, A. Sing, L. Zhang, J. L. Wrana, H. McNeill, R. Winklbauer, S. Angers, Mink1 regulates β-catenin-independent Wnt signaling via Prickle phosphorylation. *Mol. Cell. Biol.* **32**, 173–185 (2012).
27. T. Biederer, P. Scheiffele, Mixed-culture assays for analyzing neuronal synapse formation. *Nat. Protoc.* **2**, 670–676 (2007).
28. K. Onishi, R. Tian, B. Feng, Y. Liu, J. Wang, Y. Li, Y. Zou, LRRK2 mediates axon development by regulating Frizzled3 phosphorylation and growth cone-growth cone communication. *Proc. Natl. Acad. Sci. U.S.A.* **117**, 18037–18048 (2020).
29. J. Wu, M. Mlodzik, The frizzled extracellular domain is a ligand for Van Gogh/Stbm during nonautonomous planar cell polarity signaling. *Dev. Cell* **15**, 462–469 (2008).
30. T. Nagaoka, M. Furuse, T. Ohtsuka, K. Tsuchida, M. Kishi, Vangl2 interaction plays a role in the proteasomal degradation of Prickle2. *Sci. Rep.* **9**, 2912 (2019).
31. Y. Zou, Does planar cell polarity signaling steer growth cones? *Curr. Top. Dev. Biol.* **101**, 141–160 (2012).
32. K. Onishi, E. Hollis, Y. Zou, Axon guidance and injury-lessons from Wnts and Wnt signaling. *Curr. Opin. Neurobiol.* **27**, 232–240 (2014).
33. Y. Zou, Breaking symmetry - cell polarity signaling pathways in growth cone guidance and synapse formation. *Curr. Opin. Neurobiol.* **63**, 77–86 (2020).
34. B. Feng, A. Freitas, R. Tian, Y. Lee, A. Grewal, J. Wang, Y. Zou. (BioRxiv, 2020).
35. T. Nagaoka, R. Ohashi, A. Inutsuka, S. Sakai, N. Fujisawa, M. Yokoyama, Y. H. Huang, M. Igarashi, M. Kishi, The Wnt/planar cell polarity pathway component Vangl2 induces synapse formation through direct control of N-cadherin. *Cell Rep.* **6**, 916–927 (2014).
36. E. Torban, H. J. Wang, N. Groulx, P. Gros, Independent mutations in mouse Vangl2 that cause neural tube defects in looptail mice impair interaction with members of the Dishevelled family. *J. Biol. Chem.* **279**, 52703–52713 (2004).
37. B. Shafer, K. Onishi, C. Lo, G. Colakoglu, Y. Zou, Vangl2 promotes Wnt/planar cell polarity-like signaling by antagonizing Dvl1-mediated feedback inhibition in growth cone guidance. *Dev. Cell* **20**, 177–191 (2011).
38. J. Feng, Y. Xu, M. Wang, Y. Ruan, K. F. So, F. Tissir, A. Goffinet, L. Zhou, A role for atypical cadherin Celsr3 in hippocampal maturation and connectivity. *J. Neurosci.* **32**, 13729–13743 (2012).
39. S. E. Poduslo, X. Yin, J. Hargis, R. A. Brumback, J. A. Mastrianni, J. Schwankhaus, A familial case of Alzheimer's disease without tau pathology may be linked with chromosome 3 markers. *Hum. Genet.* **105**, 32–37 (1999).
40. F. Liu, A. Arias-Vasquez, K. Sleegers, Y. S. Aulchenko, M. Kayser, P. Sanchez-Juan, B. J. Feng, A. M. Bertoli-Avella, J. van Swieten, T. I. Axenovich, P. Heutink, C. van Broeckhoven, B. A. Oostra, C. M. van Duijn, A genomewide screen for late-onset Alzheimer disease in a genetically isolated Dutch population. *Am. J. Hum. Genet.* **81**, 17–31 (2007).
41. I. J. Broce, C. H. Tan, C. C. Fan, I. Jansen, J. E. Savage, A. Witoelar, N. Wen, C. P. Hess, W. P. Dillon, C. M. Glastonbury, M. Glymour, J. S. Yokoyama, F. M. Elahi, G. D. Rabinovici, B. L. Miller, E. C. Mormino, R. A. Sperling, D. A. Bennett, L. K. McEvoy, J. B. Brewer, H. H. Feldman, B. T. Hyman, M. Pericak-Vance, J. L. Haines, L. A. Farrer, R. Mayeux, G. D. Schellenberg, K. Yaffe, L. P. Sugrue, A. M. Dale, D. Posthuma, O. A. Andreassen, C. M. Karch, R. S. Desikan, Dissecting the genetic relationship between cardiovascular risk factors and Alzheimer's disease. *Acta Neuropathol.* **137**, 209–226 (2019).
42. T. Lawingco, S. Chaudhury, K. J. Brookes, T. Guetta-Baranes, R. Guerreiro, J. Bras, J. Hardy, P. Francis, A. Thomas, O. Belbin, K. Morgan, Genetic variants in glutamate-, Aβ-, and tau-related pathways determine polygenic risk for Alzheimer's disease. *Neurobiol. Aging* **101**, 299.e13–299.e21 (2020).
43. F. A. Ran, P. D. Hsu, J. Wright, V. Agarwala, D. A. Scott, F. Zhang, Genome engineering using the CRISPR-Cas9 system. *Nat. Protoc.* **8**, 2281–2308 (2013).
44. L. Swiech, M. Heidenreich, A. Banerjee, N. Habib, Y. Li, J. Trombetta, M. Sur, F. Zhang, In vivo interrogation of gene function in the mammalian brain using CRISPR-Cas9. *Nat. Biotechnol.* **33**, 102–106 (2015).
45. C. Yang, X. Wang, J. Wang, X. Wang, W. Chen, N. Lu, S. Siniossoglou, Z. Yao, K. Liu, Rewiring neuronal glycerolipid metabolism determines the extent of axon regeneration. *Neuron* **105**, 276–292.e5 (2020).
46. S. Shin, H. Pribiag, V. Lilascharoen, D. Knowland, X. Y. Wang, B. K. Lim, Drd3 signaling in the lateral septum mediates early life stress-induced social dysfunction. *Neuron* **97**, 195–208.e6 (2018).
47. P. J. Hallett, T. L. Collins, D. G. Standaert, A. W. Dunah, Biochemical fractionation of brain tissue for studies of receptor distribution and trafficking. *Curr. Protoc. Neurosci.* **Chapter 1**, Unit 1 16 (2008).
48. J. Peng, M. J. Kim, D. Cheng, D. M. Duong, S. P. Gygi, M. Sheng, Semiquantitative proteomic analysis of rat forebrain postsynaptic density fractions by mass spectrometry. *J. Biol. Chem.* **279**, 21003–21011 (2004).
49. M. Lau, "The Interaction of Enteric Bacterial Effectors with Host Engulfment Pathway Regulates Host Immune Response," thesis, University of California San Diego (2018)
50. E. Dzyubenko, A. Rozenberg, D. M. Hermann, A. Faissner, Colocalization of synapse marker proteins evaluated by STED-microscopy reveals patterns of neuronal synapse distribution in vitro. *J. Neurosci. Methods* **273**, 149–159 (2016).
51. J. L. Johnson, J. He, M. Ramadass, K. Pestonjamasp, W. B. Kiosses, J. Zhang, S. D. Catz, Munc13-4 is a Rab11-binding protein that regulates Rab11-positive vesicle trafficking and docking at the plasma membrane. *J. Biol. Chem.* **291**, 3423–3438 (2016).
52. X. Wu, Y. Zhou, Z. Huang, M. Cai, Y. Shu, C. Zeng, L. Feng, B. Xiao, Q. Zhan, The study of microtubule dynamics and stability at the postsynaptic density in a rat pilocarpine model of temporal lobe epilepsy. *Ann. Transl. Med.* **8**, 863 (2020).
53. G. Kashgari, L. Meinecke, W. Gordon, B. Ruiz, J. Yang, A. L. Ma, Y. Xie, H. Ho, M. V. Plikus, Q. Nie, J. V. Jester, B. Andersen, Epithelial migration and non-adhesive periderm are required for digit separation during mammalian development. *Dev. Cell* **52**, 764–778.e4 (2020).

Acknowledgments: We would like to thank members of the Zou laboratory for critical reading and comments on the manuscript. Airyscan confocal microscopy imaging was performed at UCSD School of Medicine Light Microscopy Facility (grant P30 NS047101). 3D STORM imaging was performed at UCSD Nikon Imaging Center (grant P30 2P30CA023100). **Funding:** This project was supported by RO1 MH116667 and R21 NS111648 to Y.Z. **Author**

contributions: Y.Z., Y.B., and T.Y. designed the experiments. Y.B., T.Y., B.F., C.L., X.W., and C.B. performed all experiments under the supervision of Y.Z. Y.B., T.Y., B.F., C.L., X.W., and Y.Z. analyzed and interpreted data. Y.B. and Y.Z. wrote the paper. All authors read and commented on the manuscript. **Competing interests:** Y.Z. is the founder of VersaPeutics and has equity, compensation, and interim managerial role. The terms of this arrangement have been reviewed and approved by the University of California, San Diego in accordance with its conflict-of-interest policies. The authors declare that they have no other competing interests. **Data and materials availability:** All data needed to evaluate the conclusions in the paper are present in the paper and/or the Supplementary Materials.

Submitted 28 February 2021
Accepted 16 August 2021
Published 6 October 2021
10.1126/sciadv.abh2974

Citation: Y. Ban, T. Yu, B. Feng, C. Lorenz, X. Wang, C. Baker, Y. Zou, Prickle promotes the formation and maintenance of glutamatergic synapses by stabilizing the intercellular planar cell polarity complex. *Sci. Adv.* **7**, eabh2974 (2021).